UNIVERSITÀ DI SIENA 1240

Dipartimento di Biotecnologie Mediche

Dottorato in Biotecnologie Mediche
35° Ciclo

Coordinatore: Prof. Lorenzo Leoncini

Titolo della tesi

Experimental evaluation of tactile sensors for oral and maxillofacial surgery

Settore scientifico disciplinare: Med /29

Candidato

Dr. Guido Gabriele

Dipartimento di biotecnologie mediche Università degli studi di Siena

Supervisore

Prof. Marco Ferrari

Dipartimento di biotecnologie mediche Università degli studi di Siena

Anno accademico di conseguimento del titolo di Dottore di ricerca
2020/21

Università degli Studi di Siena
Dottorato in BIOTECOLOGIE   MEDICHE
35° Ciclo

Data dell'esame finale
13/2/2023

Commissione giudicatrice

- Marco Rinaldo Oggioni – Professore Ordinario, Dipartimento di Farmacia Biotecnologie, Università di Bologna **marcorinaldo.oggioni@unibo.it**
- Riccardo Manganelli – Professore Ordinario, Dipartimento di Medicina Molecolare, Università di Padova, **riccardo.manganelli@unipd.it**
- Luigi Generali – Professore Associato, Dipartimento Chirurgico, Medico, Odontoiatrico e di Scienze Morfologiche, Università di Modena e Reggio Emilia, **lgenearali@unimore.it**
- Lucia Pallecchi – Professoressa Associata, Dipartimento di Biotecnologie Mediche, Università di Siena, **lucia.pallecchi@unisi.it**
- Francesco Dotta – Professore Ordinario, Dipartimento di Medicina, Chirurgia e Neuroscienze, Università di Siena, **francesco.dotta@unisi.it**
- Simone Grandini – Professore Ordinario, Dipartimento di Biotecnologie Mediche, Università di Siena, **simone.grandini@unisi.it**
- Gianni Pozzi – Professore Ordinario, Dipartimento di Biotecnologie Mediche, Università di Siena, **gianni.pozzi@unisi.it**
- Francesco Iannelli – Professore Ordinario, Dipartimento di Biotecnologie Mediche, Università di Siena, **francesco.iannelli@unisi.it**
- Marco Ferrari - Professore Ordinario, Dipartimento di Biotecnologie Mediche, Università di Siena, **marco.ferrari@unisi.it**

Supplenti

- Jean Denis Docquier – Professore Associato, Dipartimento di biotecnologie mediche, Università di Siena, **jddcquier@unisi.it**
- Maurizio Zazzi – Professore Ordinario, Dipartimento di Biotecnologie Mediche, Università di Siena, **maurizio.zazzi@unisi.it**

Foreword

The sense of touch is fundamental in surgery. It provides information about the clinical condition of tissues and feedback for controlling surgical gestures. In the last decade the use of sophisticated and low-invasive surgical techniques has limited the interaction of surgeons via their own hands. In fact the introduction of laparoscopic, endoscopic and robotic surgery has reduced the invasiveness of procedures of but also the possibility of direct control and palpation. Despite the clinical evidence on the advantages and added value of such new surgical technologies, the lack of tactile interaction remains a limiting factor. The role of tactile information concerns sensing, for example, the pressure necessary to incise a tissue or to tighten the knot of a suture or the palpation of an anatomical structure. Traditionally, tactile information is received by the own hand of the operator or through the surgical instrumentation. In fact, palpation using hands has always been a prominent part of the objective examination, allowing the physician to determine the location of pathological conditions that escape sight. In addition, it also provides information about extension, consistency and pain of hidden pathologies. Each tissue has its own tactile peculiarities as well as each procedure requires specific tool-tissue interaction. Errors in a surgical procedure due to the lack of tactile information or inadequate tool-tissue interaction forces are common and, therefore, acquiring this kind of knowledge is paramount to enhance surgical performance and education. The scope of this dissertation is to provide the state of the art in surgery and to propose a new generation of surgical tools, empowered with an artificial sense of touch for the operator. The present work has been developed and written with Dr. Pietro Navalesi and Prof. Calogero Maria Oddo , Scuola Superiore Sant'anna, Pisa. I'm grateful to them for the precious opportunity of collaboration

Table of content:

1. Introduction

Computer Assisted Surgery (CAS) has introduced several benefits in surgical practice and training, compared to traditional surgery (Figure 1-2). On the other hand, technological limitations include high cost, slow learning curve and long setup times. In particular maxillofacial surgery requires high accuracy, stability and transversal skills ranging from dentistry to general medicine (3). Robot assisted systems employed in dental and maxillofacial surgery could reduce risks for patients allowing some advantages like improving position and orientation of surgical tools, prevention of injuries to nerves and vessels in neck/head region avoiding accidental damages due to human factors at the same time. Additionally, it is demonstrated that a shortage of haptic feedback in commercial surgical tools and platforms lead to a decrease in surgeon's skills (4). Haptic ùfeedback requires ad hoc tactile sensors to acquire haptic information, tools able to integrate them and interfaces to display information or let the user feel sensations (5, 6). Tactile and force feedback is desirable to avoid injuries due to excessive applied forces when the tool-tissue interactions fall below the human sensory threshold (1), to facilitate novices learning while performing a complex or new task, to improve soft tissues/membranes manipulation and restore natural haptic feedback lost because surgeon cannot manipulate the instruments directly (7). Therefore, the research had pointed to novel tactile sensors and sensorized tools development able to be integrated in commercial existing surgical platforms. Some authors reported potential benefits and limits of haptic feedback in robot-assisted minimally invasive surgery (RMIS) as well as in head and neck surgery (4, 7, 8) reaching the same conclusions: commercial existing systems are not able to provide haptic sensations, clinical trials are mostly nonrandomized hence the necessity of randomized clinical trials to validate benefits of this technology and a cost-benefit analysis should be always considered to assess extra costs related to haptic technologies. Literature is not completely one-sided evaluating haptic feedback essential in CAS systems (9, 10) with the assumption that surgeon's experience and visual feedback alone can balance the lack of haptic feedback in RMIS practice. However, effectiveness and necessity of an integrated haptic feedback is proved in fields of application like retinal and ENT microsurgery (11, 12), endovascular treatments (13), neurosurgery and magnetic resonance imaging (MRI)-guided interventions (14). The major shortage of studies can be noticed in the dental and maxillofacial surgery field, with only a partially consistent literature covering haptic digital simulators and training platforms and a total absence of specifically designed tactile sensors or tools.
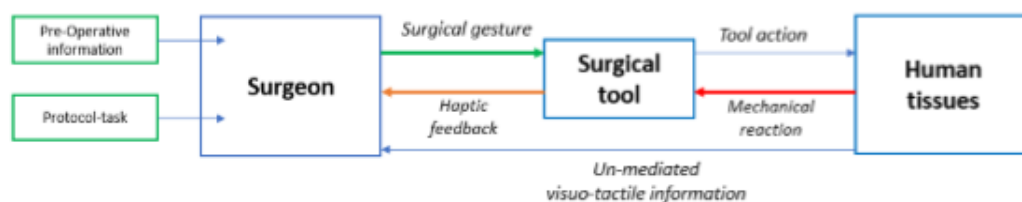
Figure 1 Traditional open-surgical process: direct manipulation and direct visual information
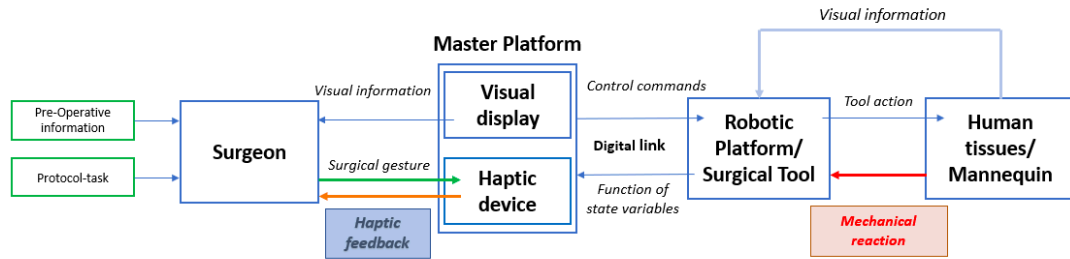

Figure 2 CAS Master-Slave surgical process: indirect manipulation and indirect visual information

1.1 Elements of human tactile physiology and main technologies to emulate human tactile sensing

1.2.1 Elements of human tactile physiology

The knowledge of human tactile systems properties is essential for an accurate and biomimetic design of tactile sensors. The human tactile system is based on unnumbered receptors, embedded in the dermis at different depths, with dissimilarities in type and functions -mechanoreceptors, thermoreceptors and nociceptors- able to obtain different contact tactile information (6, 16). Mechanoreceptors -employed in pressure and vibration stimuli detection- are classified based on receptive field's structure and rate of adaptation into Meissner corpuscles, Merkel receptors, Ruffini endings and Pacinian corpuscles. Fast adapting receptors (FA) respond to dynamic forces and vibrations with action potentials when a stimulus is provided or removed (17–19). FA-I receptors (Meissner corpuscles) present a reduced receptive field near the epidermis and measure low-frequency (5–50 Hz) stimuli; FA-II receptors (Pacinian corpuscles) have a large receptive field and measure high-frequency vibrations stimuli involved in texture discrimination and slip detection. Slowly adapting receptors (SA) respond to static pressures producing a sustained series of action potentials as long as the stimulus is in contact with their receptive fields. SA-I receptors (Merkel discs), close to the skin surface, have a tiny receptive field in the fingertips and provide high-resolution force information for object discrimination. SA-II receptors (Ruffini endings), located in the derma, have large receptive field. Main mechanoreceptors' properties and features are summarized in Table 1. Novel design tactile sensors should be "skin-like" with high sensitivity to

measure 3-D small forces (in the range 0.01-10 N), fast response (less than 1 ms) and high spatial resolution (1 mm for sensitive sites) with multimodal sensing capabilities.

Table 1: Summary of main mechanoreceptors features (Synthesis from (16–19)).

Rate of adaptation			
FA	SA		
Meissner corpuscles Small receptive field Superficially localized Detect high-frequency deformations (5-50 Hz) 140 receptors/cm^2 Spatial resolution: 3-4 mm	**Merkel receptors** Small receptive field Superficially localized Detect low-frequency deformations (<5 Hz) and static force 70 receptors/cm^2 Spatial resolution: 0.5 mm	I	*Receptive Field*
Pacinian corpuscles Large receptive field Located in depth Detect high-frequency vibrations (40-400 Hz) 20 receptors/cm^2 Spatial resolution: 10+ mm	**Ruffini endings** Large receptive field Located in depth Sensitive to skin stretch and static force 10 receptors/cm^2 Spatial resolution: 7+ mm	II	

1.2.2 Main sensing principles of tactile technologies

Transduction mechanisms of tactile transducers can be divided in two different categories: electrical-based sensors (piezoresistive, piezoelectric, capacitive, inductive sensors) and optical-based sensors (20, 21). Capacitive and inductive tactile sensors display changes in capacitance and inductance respectively. They are actually hardly used in biomedical scene because of weaknesses listed in Table 2, although the future potentialities of capacitive sensors especially in MIS. Piezoresistors show resistivity changes as a consequence of an applied force). Advantages include high spatial resolution and sensitivity while main weaknesses are low frequency response and repeatability. Strain gauge sensors consist of a resistive elastic unit and their sensing principle is based on resistance changes with strain because of shape deformation (22). Resistance variation is a function of the applied strain. Advantages include ease design and high spatial resolution while main handicaps large hysteresis and non-linear response. Piezoelectric tactile sensors transduce force/pression in a proportionally voltage (the change of electrical polarization of the piezoelectric material's element induces a mechanical deformation), but high accuracy is balanced by low spatial resolution. The optical ones, including optical fiber and FBGs sensors, obtain tactile information by analysing wavelength's changes (23, 24). An FBG sensor is a sensing element embedded into an optical fiber. FBGs sensors detect force/torque data using the variation in the FBG reflection spectrum induced by the applied load to be measure. A multicomponent FBG-based sensor should measure force/torque components along x-, y-, and z-axis. Optical sensors own unique properties essential in biomedical applications such as biocompatibility, chemical inertness, immunity to

electromagnetic interferences and high sensitivity while main limits include susceptibility to temperature, relatively high cost, complex information processing system and size limitations. As a consequence, their employment in biomedical applications is rapidly increasing.

Table 2: Summary of main tactile sensing transduction mechanisms employed in biomedical applications with advantages and disadvantages (Synthesis from (6), (20–24)).

	Sensing principle	Advantages	Disadvantages
Piezoresistors	Resistance variation	Excellent spatial resolution High sensitivity Low cost	Low frequency response Low repeatability
Capacitive sensors	Capacitance variation due to a mechanical force or moment	Temperature independent High spatial resolution High sensitivity	Crosstalk between elements Susceptible to noise Stray capacitance Hysteresis
Inductive sensors	Magnetic coupling variation due to a mechanical force or moment	High dynamic range High sensitivity Linear output	Low frequency response Poor reliability
Strain Gauges sensors	Change in resistance because of shape deformation	High spatial resolution Easy design Low cost	Large hysteresis Non-linear response
Piezoelectric sensors	Strain polarization	High accuracy High dynamic rang High frequency response	Low spatial resolution High temperature susceptibility
Optical sensors	Change in wavelength	-High spatial resolution and sensitivity - Electromagnetically inert	High temperature susceptibility High cost Size limitations

1.2.3 Main actuation principles for haptic feedback

Haptic devices, able to supply haptic feedback to the user, can be classified in two main families: grounded devices, with the base fixed to the ground, and wearable devices (25). In the following surgical applications, commercial grounded interfaces (described in detail in Chapter 7) are mainly employed with only some exception regarding novel design wearable interfaces. Grounded devices can display a vast range of forces at the expense of portability, high cost and bulk. Contrary, portable devices' strengths are wearability, low weight and volume, reduced form factor, despite of the haptic stimuli provided is still limited to vibrations with a consequent inability in reproducing complex contact interactions. To enhance the wearability of haptic interfaces, researches are focused on relocating the grounding of the system closer to the point of actuation of the stimulus although the kinesthetic component of the stimuli is reduced, preserving the cutaneous stimuli. In the borderline case, when the grounding part is coincident with the stimulus application point, the system provides only cutaneous feedback anyway without compromising tactile discrimination (26).

A possible classification of wearable haptic devices is based on haptic systems mechanical properties: Degrees of Freedom (DoF) of the end effector, workspace, precision of forces and positions rendering (describes the reproducibility of a specific action), resolution of forces and bandwidth. A fully actuated haptic device is able to render 3-Dof forces/torques, taking into account that increasing DoF number lead to a consequent increasing in design's complexity.

Haptic devices can be categorized based on action's area (fingertip or whole hand) and subdivided for type of cutaneous cues they are able to provide: normal indentation, lateral skin

stretch and vibration (vibrotactile stimuli due to vibrotactile actuators) for fingertip systems, kinesthetic or vibration for whole hand systems.

In fingertips systems based on normal indentation, actuation could be obtained using a moving system in contact with the finger pulp (27), pin arrays -with different pin diameter and pin spacing, usually moved by DC motors, servo motors, shape memory alloy (SMA) actuators, pneumatic actuators, dielectric elastomer actuators (28)- or pneumatic systems (jets and balloon-based systems). The actuation is usually due to DC motors, servomotors or SMA actuators.

Whole hand devices (also called hand exoskeletons) can provide cutaneous and kinesthetic stimuli to the entire hand. These systems employ actuation technologies used for fingertip devices but differently they can provide kinesthetic and/or pressure and/or vibration stimuli to the user. Open issues involve kinematic coupling between wearer and exoskeleton joints without meddling with wearer's motions and low wearability of systems providing kinesthetic feedback. As a solution, vibrotactile actuators with small form factor and low weight are employed to supply vibrotactile feedback instead of the kinesthetic one.

1.3 Literature review: matherials and methods

Prior to the literature search, data extraction, and analysis, the study protocol was defined under the Preferred Reporting Items for Systematic Reviews and Meta-analyses (PRISMA) statement .

The questions were formulated based on the PICO model , and record search and study selection strategies were developed. The research question focused on the study, research and/or application of haptic sensors, sensorized tools, tactile sensors and integrated platform for dentistry and maxillofacial surgery.

1.3.1 Search Strategy

Manuscript published in English of haptic sensors, sensorized tools, tactile sensors and integrated platform for dentistry and maxillofacial surgery were searched electronically through Scopus, MEDLINE/PubMed, and Cochrane Library databases by two independent reviewers (G.C., A.F.) without date restriction until 1 November 2022, using keywords and Boolean operators as follows: ("haptic" OR "sensorized" OR "tactile" OR "integrated") AND ("sensors" OR "tools" OR "platform" AND "dental" OR "dentistry" OR "maxillofacial"). No filters were applied.

1.3.2 Study Selection and Eligibility Criteria

Collected citations were recorded, duplicates were eliminated via the reference management tool EndnoteTM (Clarivate), and the remaining were screened by the three independent reviewers (FDS, FDA, MPDP), who then screened relevant abstracts. The full texts of these potentially eligible title-abstracts were obtained, contacting the study authors if full texts were unavailable, and were reviewed by the same authors . Inclusion criteria: no restrictions were applied on publication date, the number of studies, and study design included; Exclusion criteria: non-English language studies.

1.3.3 Data Extraction and Collection

Data were extracted independently and in duplicate using a standardized data extraction form developed based on the models recommended for intervention reviews of RCTs and non-RCTs before data extraction .

1.3.4 Data Synthesis

A narrative synthesis of the data regarding the population studied, intervention(s), and outcomes was performed.

The studies have been categorized in four different areas based upon the presented technologies and surgical district of employment with specific attention to maxillofacial/dental applications:

• Tactile sensors for instrumented tools

• Sensorized tools for contact forces detection

• Haptic interfaces for remote tactile feedback

• Integrated platforms for surgery and telemedicine

1.4 Results

After searching electronic databases, 7565 original manuscripts were retrieved as shown in figure 1. After applying inclusion/exclusion criteria, 31 articles have been included in the present review (17-47). A qualitative synthesis of the results have been made as reported.
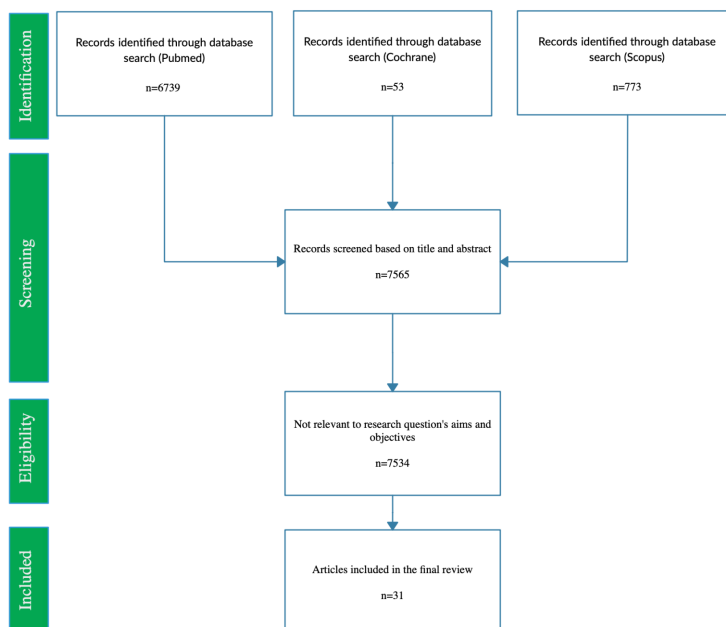
PRISMA diagram resembling article selection process from identification to inclusion.

1st Author, year	Country	Type	Field	Subjects	Category	Original technology	Conclusions
Arikatla 2020	USA/ India	CR	Orthognatic surgery	1	Integrated platforms	NA	In the future, we will employ the methods proposed in this paper to build a prototype that simulates the full procedure of the BSSO.
Bandari 2016	Canada	Review	MIS and RMIS	NA	TS-IT	NA	There is a relatively small number of recent developments of hybrid sensors for MIS and RMIS.
Bugdadi 2018	Canada	Experimental	Neurosurgery	6*	Haptic feedback; Integrated platforms	NA	To maximize realism of the training experience, educators employing virtual reality simulators may find it useful to assess expert opinion before choosing a force feedback device.
Chen 2018	China	Experimental	Dentistry	NR	Haptic feedback; Integrated platforms	DISS	The DISS may provide an alternative training method for the surgeons to enhance their dental implant surgical skills and experiences.
Dahiya 2010	Italy	Review	Translational	NA	TS-IT	NA	Much work needs to be done at the system level before artificial touch can be used in a real-world environment.
Frediani 2014	UK/Italy	Experimental	Translational	NR	Haptic feedback	bubble like HC-DEA	A novel tactile display able to simulate contact with virtual soft bodies via soft interfaces, offering low weight, no acoustic noise, no heating, scalability, and low power consumption.
Giri 2021	Canada	Review	Translational	NA	Haptic feedback	NA	The medicinal world is still skeptical about the usage of haptic devices in surgeries and training.

Girod 2015	USA	Experimental	Maxillo-facial	10**	Haptic feedback; Integrated platforms	Geomagic Touch, 3D Systems	Our advanced haptic surgical planning system enabled surgeons to simulate mandibular fracture repair more accurately and with a better user experience than a CAD system.
Hoshyar manesh 2021	Canada	Experimental	MIS and RMIS	NR	Haptic feedback; Integrated platforms	neuroArm PLUS	This manuscript describes the engineering principles behind the design and development of a microsurgery-specific haptic interface. Establishing its clinical use is outside the scope of this work.
Kim 2020	Korea	Experimental	FESS	NR	Haptic feedback; Integrated platforms	VR haptic platform	VR haptic simulators can improve the skill and confidence of surgical trainees by allowing them to accrue experience in various tasks under different conditions.
Liang 2018	China/ Canada	Review	Translational	NA	TS-IT	NA	Significant improvements have been achieved in addressing numerous aspects of designing and developing multi-component opto-electric force sensing systems.
Liu 2012	China	Experimental	Maxillo-facial	NA	ST-CFD	Control System for CMF Robot	The repeatability accuracy experiment showed that the movement of the robot is smooth, stable and safe.
Lo presti 2020	Spain/Portugal/Italy/USA/ Kazakhstan	Review	Translational	NA	TS-IT	NA	The considerable amount of attention given to FBGs in scientific papers and the growing market interest regarding their applications in medicine underline the strong interest to fulfill the gap between research and clinical practice.

Maliha 2018	USA	Review	Maxillo-facial	NA	Haptic feedback	NA	Although seemingly beneficial to the trainee in maxillofacial surgery, simulation in education in this field is an underused commodity because of the significant lack of scientific and validated study designs reported on in the literature thus far.
Medellìn-Castillo 2016	Mexico/UK	Experimental	Maxillo-facial	21**	Haptic feedback	NA	A haptic-enabled approach is feasible in 2D, $2\frac{1}{2}$D and 3D environments and that benefits were obtained in the reduction of measurement errors, lower variability and reduced task completion times.
Mencattelli 2014	Italy	Experimental	Dentistry	2	ST-CFD	customized measuring platform	This measuring system allows measurements of 6 orthodontic forces exerted by any orthodontic device.
Nicot 2017	France	CR	Maxillo-facial	1	Haptic model	NA	The description of defects through haptic 3D printed models may be a next step in the provision of parental information.
Nilsson 2020	Denmark/Sweden	Retrospective	Maxillo-facial	12	Haptic feedback	NA	In this study, we present an in-house haptic assisted planning tool with high usability that can be used for pre-operative planning and evaluation of complex mandible fractures.
Olsson 2013	Sweden	CR	Maxillo-facial	1	Haptic feedback		Preliminary testing with one surgeon indicates that our haptic planning system has the potential to become a powerful tool that with little training allows a surgeon to complete a complex CMF surgery plan in a short amount of time.

Pacchierotti 2015	Italy	Experimental	Translational	15	Haptic feedback	3-DoF cutaneous haptic device	Cutaneous feedback showed better performance than employing no force feedback at all, but, as expected, it was outperformed by full haptic feedback provided by grounded haptic interfaces.
Pacchierotti 2015b	Italy/USA	Experimental	Translational	18	Haptic feedback	SynTouch BioTac	Subjects who used a dragging strategy achieved even better results with cutaneous feedback of fingertip vibrations. Subjects also highly preferred conditions providing cutaneous feedback over the one without any haptic feedback.
Pacchierotti 2017	France/Chile/Italy	Review	Translational	NA	Haptic feedback	NA	The "wearables" technology trend will continue to play a strong role in pushing haptics forward throughout the coming decade.
Prattichizzo 2013	Italy	Experimental	Translational	14	Haptic feedback	novel 3-DoF wearable display	In comparison to similar existing cutaneous devices, this one has three actuated degrees of freedom and it is able to simulate a contact force with general direction at the fingertip.
Saccomandi 2014	Italy	Review	Translational	NA	TS-IT	NA	The growing and continuous research in the field of tactile sensing for biomedical application will go towards the fusion of many technologies, aiming to enhance the pros of each technique.
Shujaat 2021	Belgium/Sweden	CR	Orthognatic surgery	1	Haptic feedback	NA	Our findings provide evidence on the anatomical and haptic quality 3D models with various printers which may allow us to guide physicians and trainees to select a certain printer and material depending on the task

							at hand for improving surgical planning and clinical training.
Syed 2013	China	Experimental	Maxillo-facial	NR	Haptic feedback	6-DOF	The repeatability experimental results show that the movement of the manipulator under the satisfactory boundaries, which is suitable and fulfills the needs of the surgery.
Wu 2014	China	Experimental	Maxillo-facial	25**	Haptic feedback	VR-MFS	The VR-MFS provides an efficient and cost-effective way to train maxillofacial novices.
Zaragoza-Siqeiros 2019	Mexico/ UK	CR	Orthognatic surgery	6**	Haptic feedback; Integrated platforms	OSSys	The proposed system integrates the four main stages of the traditional OGS planning process: clinical facial analysis, cephalometric analysis, model surgery, and surgical template generation.
Zhang 2012	China	Experimental	Dentistry	NR	Haptic feedback	digital VR simulator	This paper presents an effective framework to simulate the pilot-drilling procedure of the micro-implants surgery.
Zhang 2015	China	Experimental	Maxillo-facial	NR	Haptic feedback		This system provides training to medical students, and can also be used in preoperative planning.
Zhang 2021	China	Experimental	Maxillo-facial	10**	Haptic feedback		There are still a lot of technical challenges in the devel- opment of virtual surgery.

Abbreviations: CAD (Computer-Aided Design); CMF (Cranio Maxillo-facial); CR (Case Report); DISS (Dental Implant Surgery Simulator); FESS (Fiberoptic Endoscopic Sinus Surgery); HC-DEA (hydrostatically coupled dielectric elastomer actuators); MIS (Minimally Invasive Surgery); NA (Not Aplicable); NR (Not

Reported); OGS (Orthognatic Surgery); RMIS (Robotic Minimally Invasive Surgery); ST-CFD (Sensorized tools for contact forces detection); TS-IT (Tactile Sensors for Instrumented Tools).

Legend: *Neuro Touch expert's Surgeons; **resident trainee in oral/maxillofacial surgery or plastic surgery with no prior experience with haptic systems

1.5 Tactile sensors for instrumented tools: dentistry and maxillofacial applications

Transduction mechanisms of tactile transducers can be divided in two different categories: electrical-based sensors (piezoresistive, piezoelectric, capacitive, inductive sensors) and opticalbased sensors (17, 18). Capacitive and inductive tactile sensors display changes in capacitance and inductance respectively. They are actually hardly used in the biomedical scene because of weaknesses listed in Table 2, although the future potentialities of capacitive sensors, especially in MIS. Piezoresistors show resistivity changes as a consequence of an applied force. Advantages include high spatial resolution and sensitivity while main weaknesses are low frequency response and repeatability. Strain gauge sensors consist of a resistive elastic unit and their sensing principle is based on resistance changes with strain because of shape deformation (19). Resistance variation is a function of the applied strain. Advantages include ease design and high spatial resolution while main handicaps large hysteresis and non-linear response. Piezoelectric tactile sensors transduce force/pression in a proportionally voltage (the change of electrical polarization of the piezoelectric material's element induces a mechanical deformation), but high accuracy is balanced by low spatial resolution. The optical ones, including optical fiber and Fiber Bragg Grating (FBG) sensors, obtain tactile information by analysing wavelength's changes (20, 21). An FBG sensor is a sensing element embedded into an optical fiber. FBGs sensors detect force/torque data using the variation in the FBG reflection spectrum induced by the applied load to be measured. A multicomponent FBG-based sensor should measure force/torque components along the x-, y-, and z-axis. Optical sensors have unique properties essential in biomedical applications such as biocompatibility, chemical inertness, immunity to electromagnetic interference and high sensitivity while main limits include susceptibility to temperature, relatively high cost, complex information processing system and size limitations. As a consequence, their employment in biomedical applications is rapidly increasing.

	Sensing principle	Advantages	Disadvantages
Piezoresistors	Resistance variation	Excellent spatial resolution High sensitivity Low cost	Low frequency response Low repeatability
Capacitive sensors	Capacitance variation due to a mechanical force or moment	Temperature independent High spatial resolution High sensitivity	Crosstalk between elements Susceptible to noise Stray capacitance Hysteresis
Inductive sensors	Magnetic coupling variation due to a mechanical force or moment	High dynamic range High sensitivity Linear output	Low frequency response Poor reliability
Strain Gauges sensors	Change in resistance because of shape deformation	High spatial resolution Easy design Low cost	Large hysteresis Non-linear response
Piezoelectric sensors	Strain polarization	High accuracy High dynamic rang High frequency response	Low spatial resolution High temperature susceptibility
Optical sensors	Change in wavelength	-High spatial resolution and sensitivity - Electromagnetically inert	High temperature susceptibility High cost Size limitations

Table 2 Summary of main tactile sensing transduction mechanisms employed in biomedical applications with advantages and disadvantages (Synthesis from (6), (20–24)).

1.6 Sensorized tools for contact forces detection: dentistry and maxillofacial applications

Maxillofacial surgery interventions are complex due to different types of anatomical structure in restricted surgical fields, each of them requiring specific procedures and appropriate skills. Moreover, esthetical appearance is essential for patients and must be considered evaluating postoperative results. Nowadays, maxillofacial procedures are performed manually for the majority, using different tools (e.g. pincers, drill, saw) -with limitations related to the intervention's duration (often more than eight hours), tiredness of surgeon, high desired accuracy in bone positioning- trying to minimize tissue and vessels' damages (22). Regarding cleft lip/palate diagnosis in unborn children, a 3D printed custom haptic model is presented by Nicot (23). This model allows surgeons to have a realistic idea of a child's anatomy as well as to perform a preoperative planning with high accuracy. In orthodontics' field an open issue is to detect and measure loads and forces applied during treatments performed with different tools in order to prevent damages. To solve this problem a customized measuring system, able to reveal forces in a range between 0.1 and 2 N, was designed by Mencattelli (24). Sensing unit is composed of 6 load cells each coupled with a strain gauge.

1.7 Main actuation principles for haptic feedback: Dentistry and maxillofacial applications

Haptic devices, able to supply haptic feedback to the user, can be classified in two main families: grounded devices, with the base fixed to the ground, and wearable devices (25). In the following surgical applications, commercial grounded interfaces are mainly employed with only some exceptions regarding novel design wearable interfaces. Grounded devices can display a vast range of forces at the expense of portability, high cost and bulk. Contrary, portable devices' strengths are wearability, low weight and volume, reduced form factor, despite the haptic stimuli provided is still limited to vibrations with a consequent inability in reproducing complex contact interactions. To enhance the wearability of haptic interfaces, researches are focused on relocating the grounding of the system closer to the point of actuation of the stimulus although the kinesthetic component of the stimuli is reduced, preserving the cutaneous stimuli. In the borderline case, when the grounding part is coincident with the stimulus application point, the system provides only cutaneous feedback anyway without compromising tactile discrimination (26). A possible classification of wearable haptic devices is based on haptic systems mechanical properties: Degrees of Freedom (DoF) of the end effector, workspace, precision of forces and positions rendering (describes the reproducibility of a specific action), resolution of forces and bandwidth. A fully actuated haptic device is able to render 3-Dof forces/torques, taking into account that increasing DoF number leads to a consequent increase in design's complexity. Haptic devices can be categorized based on action's area (fingertip or whole hand) and subdivided for type of cutaneous cues they are able to provide: normal indentation, lateral skin stretch and vibration (vibrotactile stimuli due to vibrotactile actuators) for fingertip systems, kinesthetic or vibration for whole hand systems. In fingertips systems based on normal indentation, actuation could be obtained using a moving system in contact with the finger pulp (27), pin arrays -with different pin diameter and pin spacing, usually moved by DC motors, servo motors, shape memory alloy (SMA) actuators, pneumatic actuators, dielectric elastomer actuators (28)- or pneumatic systems (jets and balloon-based systems). The actuation is usually due

to DC motors, servomotors or SMA actuators. Whole hand devices (also called hand exoskeletons) can provide cutaneous and kinesthetic stimuli to the entire hand. These systems employ actuation technologies used for fingertip devices but differently they can provide kinesthetic and/or pressure and/or vibration stimuli to the user. Open issues involve kinematic coupling between wearer and exoskeleton joints without meddling with wearer's motions and low wearability of systems providing kinesthetic feedback. As a solution, vibrotactile actuators with small form factor and low weight are employed to supply vibrotactile feedback instead of the kinesthetic one.

Haptic interfaces are widely used in dental and maxillofacial surgery especially for digital simulation purposes. A dental implant surgery simulator (DISS), based on the haptic device Omega.6 (Force Dimension, Switzerland) and CHAI3D software, is proposed in (29). Driller diameter and drill speed are variable during simulation, conducted on patient specific virtual models. Users wear 3-D glasses to receive visual feedback too. A voxel-based approach to reconstruct oral tissues and an analytical drilling force model for haptic simulation of micro-implants procedure are proposed in (30). The aim is to train orthodontists in this common procedure minimizing risks for patient's tooth roots and providing a real-time force feedback from different tissue layers. Surgeons must be careful to apply appropriate forces performing procedures like Bilateral Sagittal Split Osteotomy (BSSO), the most common mandibular intervention, which requires cutting the mandible through burr and oscillating saw. BSSO simulator (31) provides the visual feedback to the user with Occulus Rift HMD and force feedback through Geomagic Touch haptic device. Prototyping of interactive virtual environments is implemented with the interactive medical simulation toolkitiMSTK. Wu et al. (32) implemented a multimodal (visual, touch, sound) VR training system for Le-Fort I osteotomy with virtual 3D models of anatomic structures reconstructed from CT patient's data. Hardware architecture is composed of a 3D Display 300 (SenseGraphics, Switzerland), 2D LCD monitor and a force feedback haptic device Omega.6. VS2008 is the Integrated Development Environment software (Microsoft, Washington, USA) and CHAI3D (Stanford, USA) allows the communication with the haptic manipulator. Omega.6 doesn't provide torque feedback and maximum force detected during simulation is only 12 N, lower than typical forces commonly used, thus a novel haptic device is required. Common procedures in maxillofacial surgery like open reduction and palate fixation can be performed using the digital VR simulator proposed by Zhang et al. (33). In cranio-maxillofacial surgery an important issue is to restore normal skeletal anatomy in patients with complex and massive traumas. Regarding reduction of maxillary fractures and facial traumas, novel training visuo-haptic simulators have been developed (34, 35). In (34), Geomagic Phantom (3D Systems, Rock Hill, USA) desktop haptic device (providing 6-DOF input and 3-DOF force output) and CHAI 3D software allow it to operate in the 3D virtual environment with haptic sensations. A Lenovo thinkpad workstation (Beijing, China) is used to simulate the immersive scenario. To solve the issue of low maximum output force (7,9 N) related to Geomagic, authors set different levels of force feedback to allow users to feel changes in motions (35). The authors highlighted better user experiences, intuitiveness, and post-operative results of Computer Assisted Surgical (CAS) systems compared to Computer-aided design (CAD) systems used in bone fractures reduction, providing the sense of touch to users. Additionally, it's proved that appropriate pre-operative planning systems cause a reduced operating time and morbidity in patients who need this operation (36). Olsson et al. proposed a new surgery pre-operative planning system with visuo-haptic feedback regarding bone fragments reconstruction (37). Medellin-Castillo et al. deal with the topic of cephalometry (38, 39). They demonstrated 3D cephalometry significantly reduces landmarking errors compared to 2D methods and proposed a haptic VR system involving cephalometry analysis reducing bias versus traditional approach. Should be kept in mind that force feedback on different devices don't influence simulation's performances in a significant way like Bugdadi's work assess (40). Despite the growing relevance of haptic

simulators due to several advantages in oral and maxillofacial application these devices are underused too, probably because of the lack of scientific studies reported on in literature (41). The main future challenge will be to provide appropriate real-time haptic sensations during simulation and research should be directed in this direction.

1.8 Integrated Platforms for surgery and telemedicine: dentistry and maxillofacial applications

Computer assisted surgery had boundless progress in a short time, realizing improvements for patients and surgeons thanks to an increasing use of robotic platforms for surgery (1). In the following sections main robotic platforms have been reviewed, including mannequin simulators (surgical tool-target physical interactions) with haptic feedback for dentistry-maxillofacial surgery.

Haptic devices let a user interact with a real remote object/structure or with a computer generated environment, providing a sense of tangibility -called haptic feedback- (42) stocked by the device's actuators. A haptic device is a robot with a different number of degrees of freedom (DOF) -depending from structure and design- located at a control station and moved directly by the operator (43) in order to give feedback on movements and forces imposed by the user himself. The haptic tool can provide tactile feedback due to mechanoreceptors, kinesthetic feedback due to muscle tensions or rarely thermal feedback. A haptic interface is a two-way device: the user manoeuvres the haptic device and commands are sent to the robotic end-effector; meanwhile the tool-tissue contact forces are detected with force/torque sensors and sent back to the haptic device. During years numerous commercial grounded haptic devices have been proposed trying to satisfy the demanding requests in terms of huge workspace, kinematic isotropy and force/torque provided. Some of commercial haptic devices usually employed for surgical applications have been developed by Force Dimension (Omega 3, Omega 6, Omega 7 devices able to provide force feedback with 3, 6, 6+1 DOF respectively), SensAble Technologies (Phantom Omni, Phantom Desktop supplying force feedback with 3/6 DOF), Moog FCS Robotic (HapticMaster with 3 DOF), Novint (Novint Falcon™ with 3 DOF) and Entact Robotics (Entact W5D with 5 DOF). Main current limits related to these technologies are the reduced workspaces, different from conventional surgery, and lack of specificity. Given these limitations, surgeons must adapt gestures and movements to the instrument's structure, the direct line of sight between surgeon and device could induce distractions as well as holding a rigid and bulky object can lead to surgical errors.

Surgical simulators were introduced for the first time in the 1990s with the aim to simulate immersive and specific scenarios and simplify training for complex surgical procedures (41). Novel simulators employ multimodal (visual, touch, sound) virtual reality (VR) in order to improve training with countless advantages. VR simulators are cost effective, easy to use, can automatically assess surgeon's performances and provide objective feedback measures as well as enhance the strength, speed and dexterity (31). Moreover, they allow to overcome limits of traditional simulation like cost and availability of animal or cadaveric models and time-consuming practice under the supervision of experienced surgeons as well as the reduced biomimetic of physical simulators. These evaluations contributed to the growth of mannequin and digital VR simulators. Incorporating haptic feedback into VR training systems will obtain better results in terms of performance accuracy, safety, skills acquisition and learning speed (5). Main digital/physical simulators presented in our review are summarized in Table 2 based on the surgical application's field.

The first robotic assisted maxillofacial intervention in animal models was executed in 2003. Transoral Robotic Surgery (TORS) became a disruptive surgical technique with the FDA approval of the Da Vinci Surgical System for TORS (Intuitive Surgical Inc, USA) in 2009. The effectiveness

of these systems was evaluated during years in terms of safety, functional outcomes, oncological outcomes, reduced post-operative complications and cost. Limitations include limited accessibility of bulky instruments, initial long setup, long operative times and lack of force feedback and tactile perception of tissues (1). This robot's first-generation was modified in 2015 with the introduction of FLEX Robotic System (Medrobotics Inc, Raynham, USA) a robotic platform with higher manoeuvrability. Nowadays robotic surgery systems are commonly employed in head and neck neoplasm resection, cleft lip and palate, fracture reduction and OSAS (the most common type of sleep apnea) treatments. However, the complete lack of haptic and force feedback in each commercial existing system must be noticed. Novel systems should be designed to allow an integration with most common commercial robotic platforms providing tactile sensations to the user. For instance, Pacchierotti (44) implemented a cutaneous feedback interface integrated on an Intuitive Surgical da Vinci Standard, able to measure contact deformations, in the end-effector of a surgical instrument. Haptic feelings are provided to the user by fingertip deformations with a significant improvement in palpation performances.

3D printed models are widely employed in physical surgical simulators for dental and maxillofacial applications enabling surgeons to understand anatomy/pathology, practicing intricate tasks too (45). Syed et al. (46) proposed a multi-arm medical platform with a 6-DoF surgical manipulator and haptic device with force feedback (Omega.6 haptic device) able to improve surgical accuracy during maxillofacial tele-operations. A pressure commercial sensor (force-torque sensor IFS50M31A25-I25) is installed on the manipulator end-effector to detect collisions and transfer the intensity value to a haptic device. A VR haptic platform for endoscopic sinus and skull base surgeries was presented by Kim (47). Platform's architecture is composed of two Geomagic Touch X haptic devices to supply haptic feedback, a monitor for visual feedback and an endoscope device.

Table 2: Simulators with haptic feedback retrieved in the present review.

	Author, Reference	Year	Medical Procedure	Type of simulator (digital or physical)	Haptic Device (grounded or wearable)	Simulation's Software/ Physical model
Dentistry	Chen et al. (91)	2018	DIS	Digital	Omega.6 (grounded)	CHAI3D
	Zheng et al. (92)	2012	Micro-implants surgery	Digital	Phantom Desktop (grounded)	–
Maxillofacial Surgery	Arikatla (90)	2018	BSSO	Digital	Geomagic Touch (grounded)	toolkit-iMSTK
	Wu et al. (93)	2014	Le-Fort I osteotomy	Digital	Omega.6 (grounded)	VS2008 CHAI3D
	Zhang et al. (95)	2015	Reduction of maxillary fractures	Digital	Geomagic Phantom (grounded)	CHAI3D
	Zhang et al. (94)	2021	Open reduction and palate fixation	Digital	Geomagic Phantom desktop X (grounded)	OpenGL
	Kim et al. (125)	2020	Endoscopic sinus and skull base surgeries	Physical	Geomagic Touch X (grounded)	Unity3D

1.9. Discussion

In this study a comprehensive review of the newest haptic technologies - tactile sensors, sensorized tools, haptic interfaces and integrated platforms for telemedicine - employed in dentistry and maxillofacial surgery is proposed. CAS introduces several benefits in surgical practice and

training, compared to traditional surgery, like improved surgeon's performances and skills, higher precision and reproducibility, reduced complications and invasiveness with better post-operative outcomes meanwhile allowing teleoperations and large-scale adequate medical treatments. Consequently, during years many efforts have been made to overcome technological limits, the main one is the complete lack of haptic/force feedback to the surgeon in master-slave systems. In particular, research has pointed to novel tactile sensors and sensorized tools' development able to be integrated in commercial existing surgical platforms. However, despite several scientific evidence in effectiveness of both force and haptic sensing, technological translation from research to clinical practice remains unfulfilled probably because of high implementation costs and design complexity. The major shortage of studies can be noticed in the dental and maxillofacial surgical field with only a partially consistent literature covering haptic digital simulators and training platforms and a total absence of specifically designed tactile sensors or tools. A research gap between dental/maxillofacial surgery and other surgical specialties like endovascular treatments, laparoscopic surgery and microsurgery is clear. In fact, by screening results of the present review we mainly found case reports and retrospective work with an absence of prospective large scale, multicentric studies and clinical trials. Furthermore, this work intends to establish -based on the literature- technological trends about haptic transducing mechanisms in surgery over the years in order to suggest the most adequate sensing principle able to be translated in maxillofacial and dental surgery's applications. Despite the major adoption in each surgical field of electrical-based tactile sensors (e.g., piezoresistive and piezoelectric tactile sensors) during the years, since the last decade the adoption of optical-based tactile sensors is growing. A preeminent adoption and development of optical and FBGs-based sensors/tools has been highlighted especially in microsurgery, endovascular procedures (48), MIS (20) and MRI-guided interventions because of unique properties essential in biomedical applications. The employment of optical and FBGs-based tactile sensors in novel tools especially designed for dental/maxillofacial surgery purposes, in light of the excellent technological results exposed in literature, could be an innovative and disruptive idea to enhance surgical performances simultaneously reducing drawbacks. To confirm this thesis additional work should be carried on especially in the unexplored field of haptic feedback in dental and maxillofacial surgery.

References

1. Wang Z, Wang S, Zuo S. 2019. A hand-held device with 3-DOF haptic feedback mechanism for microsurgery. Int. J. Med. Robot. Comput. Assist. Surg. 15(5):

2. Koehn JK, Kuchenbecker KJ. 2015. Surgeons and non-surgeons prefer haptic feedback of instrument vibrations during robotic surgery. Surg. Endosc. 29(10):2970–83

3. Liu HH, Li LJ, Shi B, Xu CW, Luo E. 2017. Robotic surgical systems in maxillofacial surgery: A review. Int. J. Oral Sci. 9(2):63–73

4. Friedrich DT, Scheithauer MO, Greve J, Hoffmann TK, Schuler PJ. 2017. Recent advances in robot-assisted head and neck surgery. Int. J. Med. Robot. Comput. Assist. Surg. 13(2):

5. Quek ZF, Provancher WR, Okamura AM. 2019. Evaluation of Skin Deformation Tactile Feedback for Teleoperated Surgical Tasks. IEEE Trans. Haptics. 12(2):

6. Chi C, Sun X, Xue N, Li T, Liu C. 2018. Recent progress in technologies for tactile sensors. Sensors (Switzerland). 18(4):

7. Okamura AM. 2009. Haptic feedback in robot-assisted minimally invasive surgery

8. Zhou M, Tse S, Derevianko A, Jones DB, Schwaitzberg SD, Cao CGL. 2012. Effect of haptic feedback in laparoscopic surgery skill acquisition. Surg. Endosc. 26(4):1128–34

9. Hagen ME, Meehan JJ, Inan I, Morel P. 2008. Visual clues act as a substitute for haptic feedback in robotic surgery. Surg. Endosc. Other Interv. Tech.

10. Meccariello G, Faedi F, AlGhamdi S, Montevecchi F, Firinu E, et al. 2016. An experimental study about haptic feedback in robotic surgery: may visual feedback substitute tactile feedback? J. Robot. Surg. 10(1):57–61

11. Iordachita I, Sun Z, Balicki M, Kang JU, Phee SJ, et al. 2009. A sub-millimetric, 0.25 mN resolution fully integrated fiber-optic force-sensing tool for retinal microsurgery. Int. J. Comput. Assist. Radiol. Surg. 4(4):383– 90

12. Bell B, Stankowski S, Moser B, Oliva V, Stieger C, et al. 2010. Integrating optical fiber force sensors into microforceps for ORL microsurgery. 2010 Annu. Int. Conf. IEEE Eng. Med. Biol. Soc. EMBC'10, pp. 1848–51

13. Wang Y, Hu K, Xiao N, Guo S. 2013. A force acquisition method in a catheter navigation system. 2013 ICME Int. Conf. Complex Med. Eng. C. 2013, pp. 633–37

14. Park YL, Elayaperumal S, Daniel B, Ryu SC, Shin M, et al. 2010. Real-time estimation of 3-D needle shape and deflection for MRI-guided interventions. IEEE/ASME Trans. Mechatronics. 15(6):906–15

15. Moher, D.; Shamseer, L.; Clarke, M.; Ghersi, D.; Liberati, A.; Petticrew, M.; Shekelle, P.; Stewart, L.A.; PRISMA-P Group. Preferred reporting items for systematic review and meta-analysis protocolss (PRISMA-P) 2015 statement. Syst. Rev. 2015, 4, 1. [CrossRef] [PubMed]

16. Liberati, A.; Altman, D.G.; Tetzlaff, J.; Mulrow, C.; Gøtzsche, P.C.; Ioannidis, J.P.; Clarke, M.; Devereaux, P.J.; Kleijnen, J.; Moher, D. The PRISMA statement for reporting systematic reviews and meta-analyses of studies that evaluate health care interventions: Explanation and elaboration. PLoS Med. 2009, 6, 1000100. [CrossRef] [PubMed]

17. Bandari N, Dargahi J, Packirisamy M. 2020. Tactile sensors for minimally invasive surgery: A review of the state-of-the-art, applications, and perspectives

18. Dahiya RS, Metta G, Valle M, Sandini G. 2010. Tactile sensing-from humans to humanoids. IEEE Trans. Robot.

19. Saccomandi, P., Schena, E., Oddo, C. M., Zollo, L., Silvestri, S., & Guglielmelli, E. (2014). Microfabricated tactile sensors for biomedical applications: a review. Biosensors, 4(4), 422–448. https://doi.org/10.3390/bios4040422

20. Liang Q, Zou K, Long J, Jin J, Zhang D, et al. 2018. Multi-Component FBG-Based Force Sensing Systems by Comparison with Other Sensing Technologies: A Review. IEEE Sens. J. 18(18):7345–57

21. Lo Presti D, Massaroni C, Jorge Leitao CS, De Fatima Domingues M, Sypabekova M, et al. 2020. Fiber bragg gratings for medical applications and future challenges: A review. IEEE Access. 8:156863–88

22. Liu TB, Duan XG, Huang Q, Zhao HH, Guo QB. 2012. Control system for maxillofacial surgery robot: Masterslave, motion control and safety design. 2012 ICME Int. Conf. Complex Med. Eng. C. 2012 Proc., pp. 203–8

23. Nicot R, Couly G, Ferri J, Levaillant JM. Three-dimensional printed haptic model from a prenatal surface-rendered oropalatal sonographic view: a new tool in the surgical planning of cleft lip/palate. Int J Oral Maxillofac Surg. 2018;47(1):44-47. doi:10.1016/j.ijom.2017.06.005

24. Mencattelli M, Donati E, Cultrone M, Stefanini C. Novel universal system for 3-dimensional orthodontic force-moment measurements and its clinical use. Am J Orthod Dentofacial Orthop. 2015;148(1):174-183. doi:10.1016/j.ajodo.2015.01.028

25. Pacchierotti C, Sinclair S, Solazzi M, Frisoli A, Hayward V, Prattichizzo D. Wearable Haptic Systems for the Fingertip and the Hand: Taxonomy, Review, and Perspectives. IEEE Trans Haptics. 2017;10(4):580-600. doi:10.1109/TOH.2017.2689006

26. Pacchierotti C, Meli L, Chinello F, Malvezzi M, Prattichizzo D. 2015. Cutaneous haptic feedback to ensure the stability of robotic teleoperation systems. Int. J. Rob. Res. 34(14):1773–87

27. Prattichizzo D, Chinello F, Pacchierotti C, Malvezzi M. Towards wearability in fingertip haptics: a 3-DoF wearable device for cutaneous force feedback. IEEE Trans Haptics. 2013;6(4):506-516. doi:10.1109/TOH.2013.53

28. Frediani G, Mazzei D, De Rossi DE, Carpi F. Wearable wireless tactile display for virtual interactions with soft bodies. Front Bioeng Biotechnol. 2014;2:31. Published 2014 Sep 1. doi:10.3389/fbioe.2014.00031

29. Chen X, Sun P, Liao D. A patient-specific haptic drilling simulator based on virtual reality for dental implant surgery. Int J Comput Assist Radiol Surg. 2018;13(11):1861-1870. doi:10.1007/s11548-018-1845-0

30. Zheng F, Lu WF, Wong YS, Foong KW. An analytical drilling force model and GPU-accelerated haptics-based simulation framework of the pilot drilling procedure for micro-implants surgery training. Comput Methods Programs Biomed. 2012;108(3):1170-1184. doi:10.1016/j.cmpb.2012.05.015

31 Arikatla VS, Tyagi M, Enquobahrie A, et al. High Fidelity Virtual Reality Orthognathic Surgery Simulator. Proc SPIE Int Soc Opt Eng. 2018;10576:1057612. doi:10.1117/12.2293690

32. Wu F, Chen X, Lin Y, et al. A virtual training system for maxillofacial surgery using advanced haptic feedback and immersive workbench. Int J Med Robot. 2014;10(1):78-87. doi:10.1002/rcs.1514

33. Zhang J, Qian J, Zhang H, He L, Li B, et al. 2021. Maxillofacial Surgical Simulation System With Haptic Feedback. J. Ind. Manag. Optim. 17(6):3645–57

34. Zhang J, Li D, Liu Q, He L, Huang Y, Li P. 2015. Virtual surgical system in reduction of maxillary fracture. Int. Conf. Digit. Signal Process. DSP. 2015-Septe:1102–5

35. Girod S, Schvartzman SC, Gaudilliere D, Salisbury K, Silva R. Haptic feedback improves surgeons' user experience and fracture reduction in facial trauma simulation. J Rehabil Res Dev. 2016;53(5):561-570. doi:10.1682/JRRD.2015.03.0043

36. Nilsson J, Nysjö F, Nyström I, Kämpe J, Thor A. Evaluation of in-house, haptic assisted surgical planning for virtual reduction of complex mandibular fractures. Int J Comput Assist Radiol Surg. 2021;16(6):1059-1068. doi:10.1007/s11548-021-02353-w

37. Olsson P, Nysjö F, Hirsch JM, Carlbom IB. A haptics-assisted cranio-maxillofacial surgery planning system for restoring skeletal anatomy in complex trauma cases. Int J Comput Assist Radiol Surg. 2013;8(6):887-894. doi:10.1007/s11548-013-0827-5

38. Medellín-Castillo HI, Govea-Valladares EH, Pérez-Guerrero CN, Gil-Valladares J, Lim T, Ritchie JM. The evaluation of a novel haptic-enabled virtual reality approach for computer-aided cephalometry. Comput Methods Programs Biomed. 2016;130:46-53. doi:10.1016/j.cmpb.2016.03.014

39. Zaragoza-Siqueiros J, Medellin-Castillo HI, de la Garza-Camargo H, Lim T, Ritchie JM. An integrated haptic-enabled virtual reality system for orthognathic surgery planning. Comput Methods Biomech Biomed Engin. 2019;22(5):499-517. doi:10.1080/10255842.2019.1566817

40. Bugdadi A, Sawaya R, Bajunaid K, et al. Is Virtual Reality Surgical Performance Influenced by Force Feedback Device Utilized?. J Surg Educ. 2019;76(1):262-273. doi:10.1016/j.jsurg.2018.06.012

41. Maliha SG, Diaz-Siso JR, Plana NM, Torroni A, Flores RL. Haptic, Physical, and Web-Based Simulators: Are They Underused in Maxillofacial Surgery Training?. J Oral Maxillofac Surg. 2018;76(11):2424.e1-2424.e11. doi:10.1016/j.joms.2018.06.177

42. Giri GS, Maddahi Y, Zareinia K. 2021. An Application-Based Review of Haptics Technology. Robotics

43. Hoshyarmanesh H, Zareinia K, Lama S, Sutherland GR. 2021. Structural design of a microsurgery-specific haptic device: neuroArmPLUSHD prototype. Mechatronics. 73(January 2020):102481

44. Pacchierotti C, Prattichizzo D, Kuchenbecker KJ. Cutaneous Feedback of Fingertip Deformation and Vibration for Palpation in Robotic Surgery. IEEE Trans Biomed Eng. 2016;63(2):278-287. doi:10.1109/TBME.2015.2455932

45. Shujaat S, da Costa Senior O, Shaheen E, Politis C, Jacobs R. Visual and haptic perceptibility of 3D printed skeletal models in orthognathic surgery. J Dent. 2021;109:103660. doi:10.1016/j.jdent.2021.103660

46. Syed AA, Duan XG, Kong X, Li M, Wang Y. 2013. Maxillofacial surgical robotic manipulator controlled by haptic device with force feedback. 2013 ICME Int. Conf. Complex Med. Eng. C. 2013, pp. 363–68

47. Kim DH, Kim HM, Park JS, Kim SW. Virtual Reality Haptic Simulator for Endoscopic Sinus and Skull Base Surgeries. J Craniofac Surg. 2020;31(6):1811-1814. doi:10.1097/SCS.0000000000006395

48. Ghamraoui AK, Ricotta JJ. 2018. Current and future perspectives in robotic endovascular surgery. Curr. Surg. Reports. 6(12):1–7

The experimental part of this work proposes a prototype of a new sensorised tool for surgery.

2. Tool design and development

2.1 Tool choice, preliminary tool design, role of Finite Element Method in engineering field

The selection of the instrument was performed by Dr.Guido Gabriele while the design and the experiments was performed by Dr. Pietro Navalesi under the supervision of Prof. Calogero Maria Oddo at Scuola Superiore Sant'anna in Pisa, Italy.

Because of the scarce presence of sensorized surgical tools addressed to maxillofacial surgery or dentistry in literature, the first step of this experimental work is the choice of a commercial surgical tool able to be sensorized.. The chosen tool should be: largely employed in maxillofacial procedures, easy to handle, with low weight and volume, space-savings, ergonomics, cheap and able to operate in the range of forces typical of maxillofacial tasks like suturing, grasping or drilling (see Chapter 1). Because of the wide range of possible tasks and consequently the wide range of

exerted forces, a skimming of candidates was carried out deciding to focus this work on grasping and palpation tools.

Moreover, a balance between surgical demands and engineering/design demands was mandatory. The chosen tool should be: feasible to be sensorized with optical FBGs-based sensors with adequate dimensions and properties, possibly low bulk, easily 3D printable in plastic or metal with an adequate complexity and ease in assembling sensors with frame.

In light of previous considerations, the choice fell on a shortlist of candidate commercial surgical forceps, whose CAD files were available on online CAD-databases like GrabCAD, CadNav, Sketchfab and Turbosquid. The final choice fell back on the surgical forceps whose preliminary CAD design (powered with Autodesk fusion 360 software) is in Figure 2.1, because of adequate dimensions, thickness and length able to permit the future integration of optical fiber sensors, adequate shape of the tip and handle for tool sensorization and manipulation.

Figure 2.1: Preliminary CAD design of the chosen surgical forceps.

The presented tool has a length of 120 mm, a mean thickness of 2 mm and a mean width of 5 mm with the maximum width at the grip and the minimum at the tip, resulting manoeuvrable and adequate to complex anatomies and inaccessible places.

The following step (described in 2.2) is a preliminary Finite Element (FE) simulation employing Autodesk Fusion 360 software and subsequently an in-dept FE simulation with Ansys Mechanical APDL software.

The Finite Element Method (FEM) is a computer-based method, employable in many fields -from industrial field to biomedical applications- able to describe, analyse and solve complex issues using numerical methods. Complex structures can be decomposed into numerous simple elements which in their entirety form the mesh. The final solution derives from the sum of the calculations carried

out by the solver for each single element. Definitely, FE simulations allow to solve and bypass the main design issues responding to various needs during prototyping with high performances and accuracy, allowing to find out best prototype properties, materials, geometries before the physical fabrication and avoiding wastes of time/money during design and test phases. These strengths lead to an increasement in efficiency and productivity. A possible weakness, identifiable in biomedical field, is model generation due to a previous lack of knowledge of the model's anatomy intended to be studied. Consequently, an intermediate step of model anatomy acquisition with magnetic resonance of computer tomography is necessary.

In this work, the forceps model with a known geometry is designed in a CAD environment and then imported in FE software.

2.2 Qualitative Finite Element Analysis

A preliminary qualitative FE analysis was carried on with Autodesk Fusion 360 software as a comparison with the following more complex and automatized simulations. The aim of this step is to emulate a gripping procedure with a force in the handle emulating the force exerted by user's fingertip and a force on the tool's tip emulating the nodule's reaction force. Manually modifying loads intensity and area of application is feasible to study parameters of interest like displacement, mechanical strain and mechanical stress in a "Static Structural" analysis.

Tool design in Figure 2.1 is directly available in the software section 'Simulation'. The process steps can be summarized in:

• _Design simplification: taking advantage from tool symmetry, simulation can be limited to a single tool side whereas the other will behave in a specular way. Moreover, a removal of non-essential design processes is powered.

• _Tool material: Commercial Aluminium 1100-O (isotropic, elastic, linear material).

• _Applied mechanical loads: A force in the range [0-10] N applied in a similar fingertip circular area of $16\pi \_mmmm2$ in the handle emulating the force exerted by user's fingertip and a force in the range [0-10] N applied in the tool tip emulating the nodule reaction force.

• _Mechanical constrains: a fixed structural constraint (x, y, z axes) on the reaction force opposite end.

Results (after a free meshing process):

• _Total mechanical displacement: Maximum at the tip, zero value on the constrain.

• _Total mechanical strain (equivalent deformation): Maximum at the tip, due to the nodule reaction force.

• _Total mechanical stress (Von Mises): Maximum at the tip, due to the nodule reaction force.
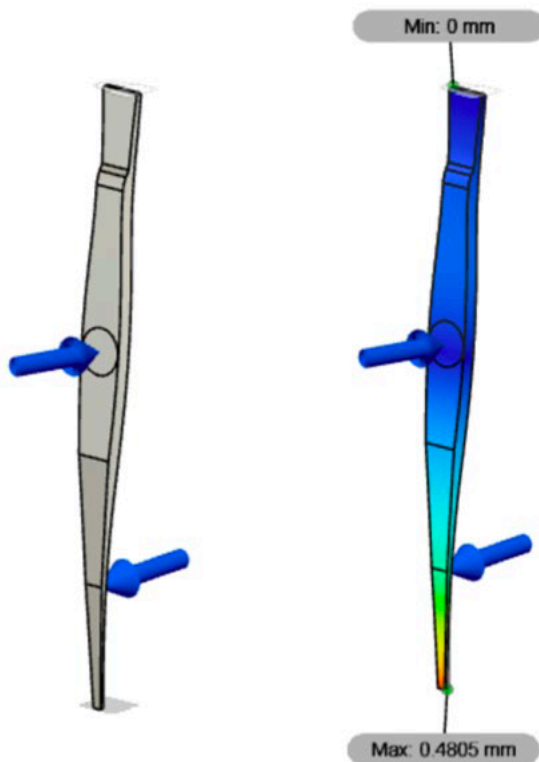
Figure 2.2: (a) Simulation's features, (b) Results: total mechanical displacement.

Subsequently, an in-depth FE static structural analysis was conducted with Ansys Mechanical APDL and Ansys Mechanical APDL Batch simulation environment for simulation process automatization. The aim of this phase is the simulation of a gripping procedure under many different input simulation conditions. The mechanical static structural analysis was carried on varying 3 input parameters:

• Force in the handle emulating the force exerted by user's fingertip, with an intensity in the range [1;5]N with a step of 1N, applied in a fingertip-similar square area of 4mm side length.

• Force on the tool tip emulating the nodule reaction force, with an intensity in the range [1;5]N with a step of 1N, applied in a nodule-similar square area of 20 μm side length.

• Square centre position along the tool major axis (z axis) in a range of [-2;0]mm with a step of 0.5 mm toward the tool middle line, in order to emulate user's fingertip position.

Definitely, there are 125 different combination of input parameters and consequently 125 different simulations derived. Regarding data extraction, the aim is to save -in different txt files- results referred to each single node of the mesh in order to feed a Neural Network.

Simulation process can be summarized as follows:

• Design adjustment and simplification: Some changes in tool design are necessary to allow the meshing step. Taking advantage from tool symmetry, simulation can be limited to a single tool side whereas the other will behave in a specular way. Moreover, a single tool side can be divided in other two symmetric sides along the tool major axis (z-axis), introducing a symmetry constraint, whereas the other will behave in a specular way. A splitting of the single resulting tool side into 10

different partitions is necessary to allow a mapped mesh in the meshing phase. The final model ready for importation is in Figure 2.3.

 • Model importation and scaling: CAD model obtained with Autodesk Fusion 360 is saved in a "iges" file, able to be imported into Ansys APDL. A scaling from metres to mm is necessary.

Figure 2.3: Final CAD model for Ansys APDL importation.

 Element type: Element type 45, describing a 4-node 3D structural solid.

 • _Material properties: Commercial Aluminium 1100-O (isotropic, elastic and linear material) with a Young Module of 69 GPa and a Poisson Module of 0,33.

 • _Meshing: Thanks to the previous splitting, a mapped mesh is implementable in each model partition (a detail of tool's tip mapped mesh in Figure 2.4).
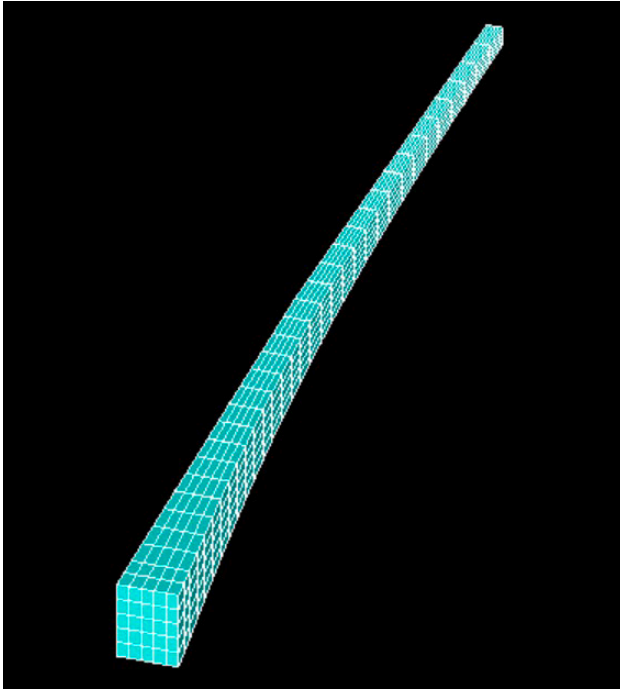
Figure 2.4: Detail of forceps 'tip mapped mesh.

• _Mechanical and symmetry constraints, mechanical loads: Because of the single tool side division along the major tool axis in two symmetrical parts a symmetry constrain along the y axis is necessary. A fixed structural constraint (x, y, z axes) -on the reaction force opposite end- is implemented too in order to guarantee system mechanical balance (Figure 2.5). Constraints are implemented in mesh nodes. Mechanical loads are described previously and implemented in mesh nodes (Figure 2.6)
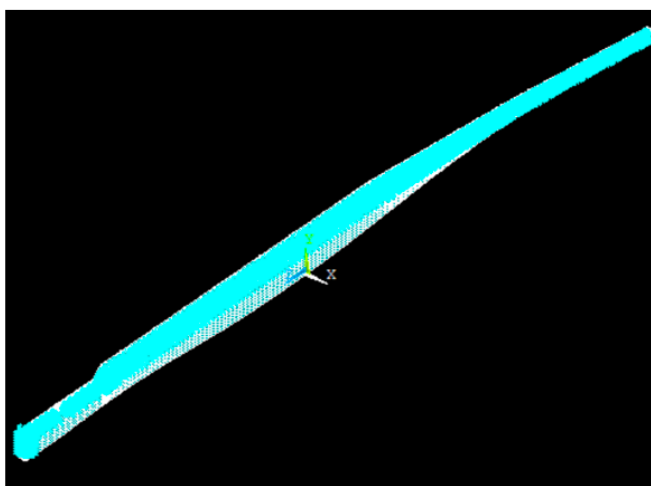
Figure 2.5: Mechanical and symmetry constrains.
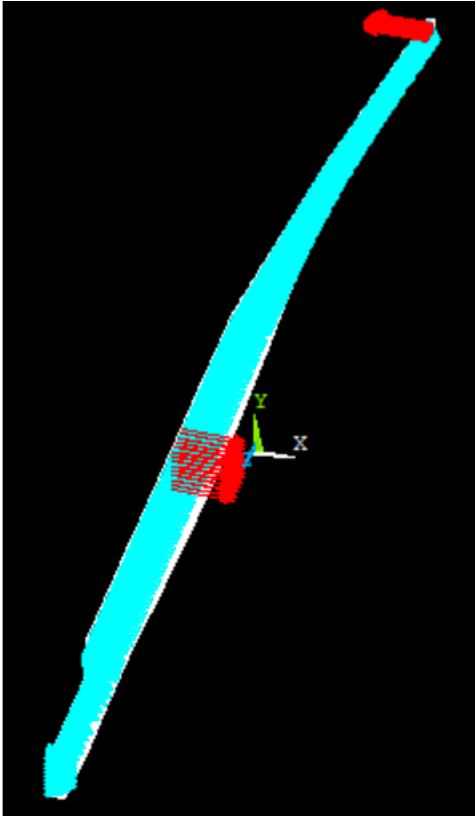
Figure 2.6: Mechanical loads (for fingertip position along z_axis=0 mm).
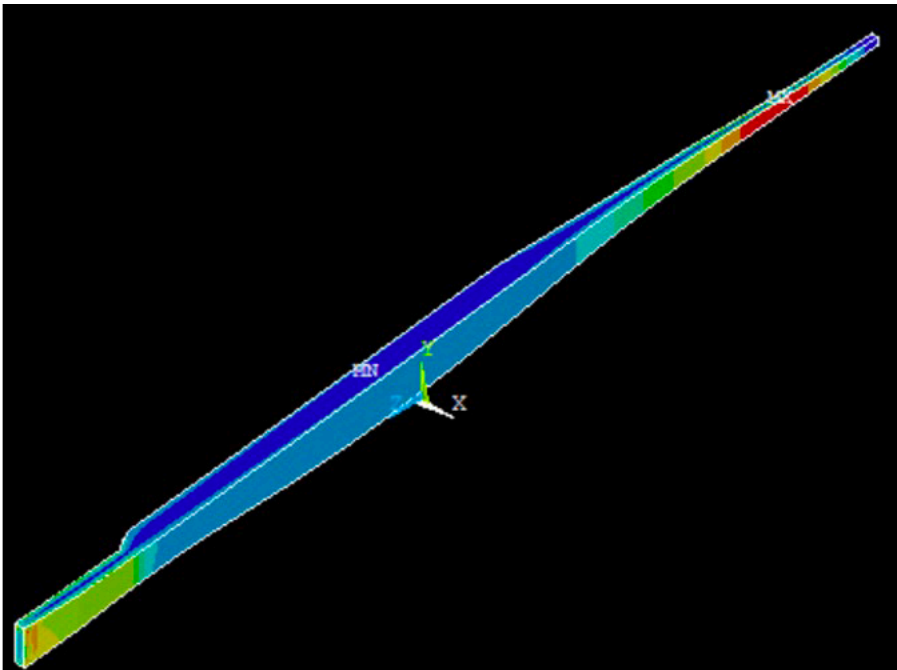
Figure 2.7: Qualitative simulation results for: (a) total displacement, (b) total mechanical von Mises strain for the input parameter combination fingertip_force=3 N, reaction_force=3 N,

fingertip position along z_axis=0 mm, (c) total mechanical von Mises stress for the same parameters combination.

We conducted a qualitative study to demonstrate the feasibility of the automatized simulation process and the relative data extraction with a complex geometry using Ansys Mechanical APDL and Ansys Batch simulation environment. In particular, the extraction involves each node of the mesh for each combination of input parameters. Saving data of every combination in a unique 'txt' file proved unmanageable, since a single 'txt' file for each result derived from a single parameters combination is recommended. Results of interest for each node of the mesh are:
• _Node number, each node of the mesh is identifiable with a unique integer and positive number.
• _Node X-coordinate, Y-coordinate, Z-coordinate, to localize spatially each node.
• _Total von Mises mechanical strain (EPTOEQV)
• _EPTOX, EPTOY, EPTOZ
• _EPTOXY, EPTOYZ, EPTOXZ
• _Total von Mises mechanical stress (SEQV), expressed in Pascal
• _SX, SY, SZ (expressed in Pascal)
• _SXY, SYZ, SXZ (expressed in Pascal)

For each input parameters combination, data extraction involves 18 results of interest for each node of the mesh.

2.3 Geometry choice, Finite Element simulation of a nodule gripping

In light of the previous dissertations, the feasibility of an automatized simulation process is demonstrated as well as an adequate data extraction. However, because of the complex model's geometry an appropriate comparison with the expected theoretical results is hard. Moreover, a reaction force with imposed intensity on forceps tip emulating the nodule reaction force could be an oversimplification of the tool-tissue contact phenomenon.

Consequently, a decisive case study could be a model-geometry simplification, replacing the original model geometry with a similar-beam geometry, meanwhile implementing a more realistic simulation of the tool-nodule contact phenomenon in the field of non-linear contacts. Instead of an imposed reaction force at the tool tip, simulations are carried out obtaining data directly from beam-nodule contacts. Hence a hemisphere of 5 mm diameter emulating the nodule is implemented.

A FE static structural analysis is conducted with Ansys Mechanical APDL and Ansys Mechanical APDL Batch simulation environment for simulation process automatization. The aim of this phase is the study and data extraction of a gripping procedure under many different input simulation conditions. The mechanical static structural analysis was carried on varying 3 input parameters:
• _Force in the handle emulating the force exerted by user's fingertip, with an intensity in the range [0;10]N with a step of 1N, applied in a fingertip-similar square area of 6 mm side length (handle_load input parameter).
• _Square centre position along the tool major axis (y axis) in a range of [-10;0]mm with a step of 1 mm toward the tool middle line, in order to emulate user's fingertip position (y_central input parameter).
• _Hemisphere centre position along the tool major axis (y axis) in a range of [57;47]mm with a step of -1 mm toward the tool tip, in order to emulate different gripping positions (y_hemisphere input parameter).

Definitely, there are 1331 different combination of input parameters and consequently 1331 different simulations derived. Regarding data extraction, the aim is to save -in different txt files- results referred to each single node of the mesh in order to feed an ad hoc Neural Network.

Simulation process can be summarized as follows:

• **_Element type:** Element type 185, 3D 8-Node Structural Solid.

SOLID185 3-D 8-Node Structural Solid 8 nodes 3-D space DOF: UX, UY, UZ	

- **Model realization and simplification:** Taking advantage from the tool symmetry, simulation can be limited to a single tool side whereas the other will behave in a specular way. A rectangular beam emulating a single side of the surgical forceps is generated directly in Ansys APDL environment as well as the hemisphere emulating the nodule. Particularly, the beam dimensions derive from the mean dimensions of the original model: beam length of 120 mm, width of 5 mm, thickness of 2 mm. Hemisphere radius is 2,5 mm while hemisphere centre is along the beam major axis (Figure 2.8).
- **Material properties:** Commercial Aluminium 1100-O (isotropic, elastic and linear material) with a Young Module of 69 GPa and a Poisson Module of 0,33 for the beam. Silicon-based material (isotropic, elastic and linear material) with Young Module of 0,003 GPa and a Poisson Module of 0,49 for the nodule.
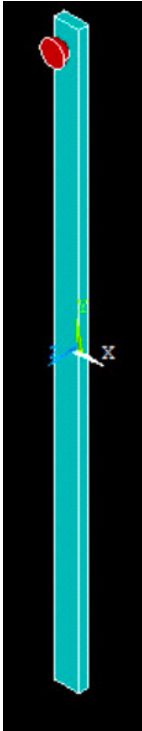
Figure 2.8: Models employed in the FE analysis (beam and hemisphere).

- **Meshing:** A mapped mesh is implemented in the beam while a free mesh is implemented in the hemisphere (Figure 2.9).
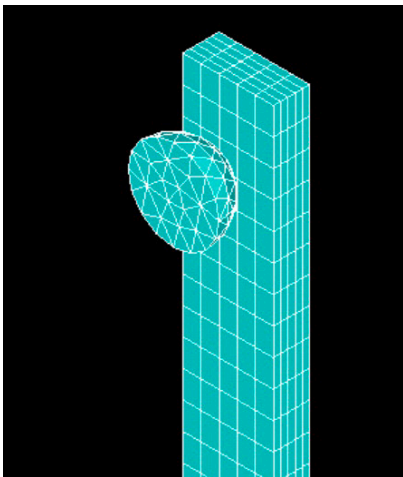
Figure 2.9: Detail of beam's mapped mesh and hemisphere free mesh.

• Implementation of mechanical contacts: This phase is initially performed with the Ansys APDL contact manager and subsequently with an ad hoc APDL code (see Appendix 2) for the automatization.

• Mechanical constraints, mechanical loads: A fixed structural constraint (x, y, z axes) -on the nodule opposite end- is implemented in order to guarantee system's mechanical balance. Another fixed structural constraint (x, y, z axes) is implemented in the base area of the hemisphere. Constraints are implemented in mesh nodes. Mechanical loads are described previously and implemented in the mesh nodes (Figure 2.10).

• Non-linear nodal solution, necessary because of the contact's implementation.
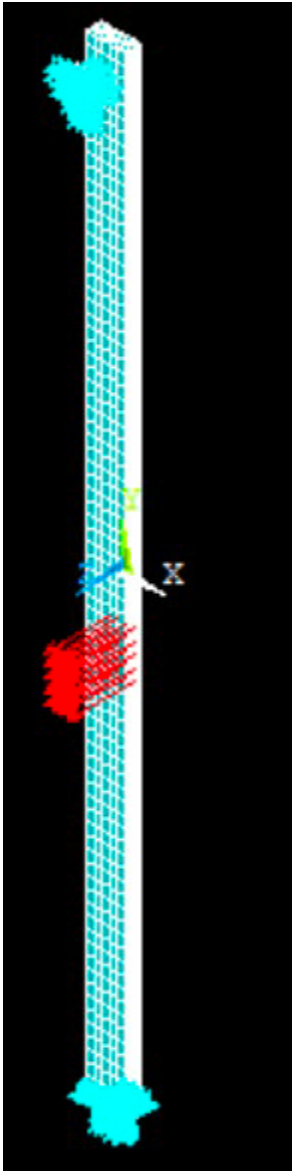
Figure 2.10: Mechanical constrains and mechanical load (for fingertip position y_central=-9mm).

Qualitative results of total displacement, total von Mises mechanical strain and total von Mises mechanical stress are presented in Figure 2.11.
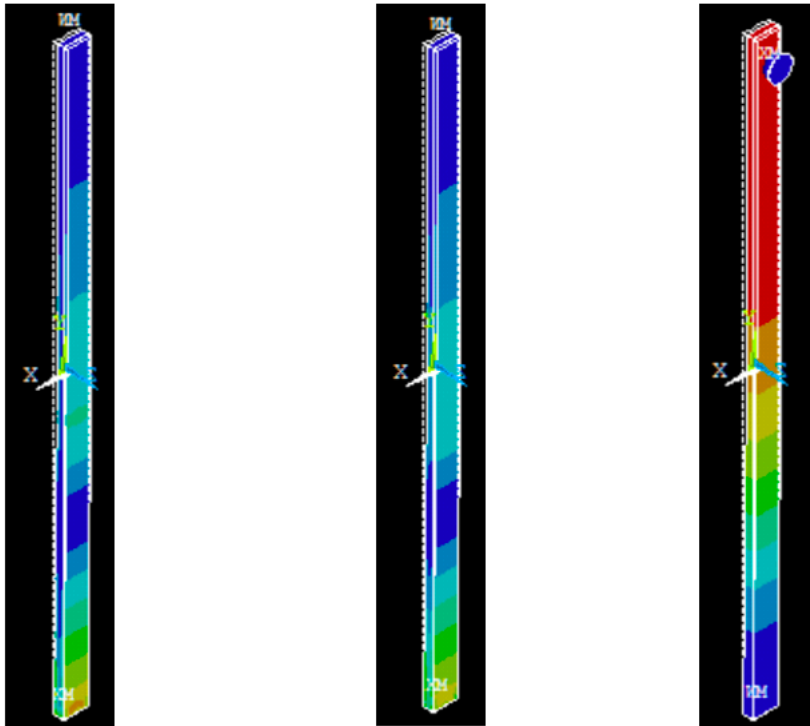
Figure 2.11: Qualitative simulation results for: (a) beam total mechanical von Mises stress, (b) beam total mechanical von Mises strain for the input parameter combination Fingertip_force=7 N, nodule position along y_axis= -1 mm, fingertip position along y_axis=-9 mm, (c) total displacement for the same parameters combination.

Subsequently, a quantitative analysis and an automatized data extraction are performed with Ansys Mechanical APDL Batch simulation environment. In particular, the extraction involves each node of the mesh for each combination of input parameters. A single 'txt' file for each result derived from a single parameters combination is recommended. Results of interest for each node of the mesh are:

• _Node number (Node ID), each node of the mesh is identifiable with a unique integer and positive number.

• _Node X-coordinate, Y-coordinate, Z-coordinate, to localize spatially each node.

• _Total von Mises mechanical strain (EPTOEQV)

• _EPTOX, EPTOY, EPTOZ

• _EPTOXY, EPTOYZ, EPTOXZ

- _Total von Mises mechanical stress (SEQV), expressed in Pascal
- _SX, SY, SZ (expressed in Pascal)
- _SXY, SYZ, SXZ (expressed in Pascal)

Definitely, there are 1331 different combination of input parameters and consequently 1331 different simulations derived whose results are saved in 1331 different 'txt' files. For each input parameters combination, data extraction involves 18 results of interest for each node of the mesh. In a single 'txt' file, numerical results are organized in a matrix representation with the number of columns equal to 21 (the number of results of interest (18, listed below) and the three-input parameter which define a specific combination P1/P2/P3) and the number of rows equal to 3054 representing the total nodes number (including hemisphere nodes). This results representation allows a profitable subsequently data analysis and management of the Neural Networks.

A model of the final matrix 3054x21 obtained at the end of the data extraction process for each parameters combination is presented below in Figure 2.12

P1	P2	P3	NODE #	X NODE	Y NODE	Z NODE	EPTO EQV	EPTO X	EPTO Y	EPTO Z	EPTO XY	EPTO YZ	EPTO XZ	SEQV	SX	SY	SZ	SXY	SYZ	SXZ
Value	Value	Value	Value	Value	Value	Value	Value	Value	Value	Value	Value	Value	Value	Value	Value	Value	Value	Value	Value	Value
Value	Value	Value	Value	Value	Value	Value	Value	Value	Value	Value	Value	Value	Value	Value	Value	Value	Value	Value	Value	Value
Value	Value	Value	Value	Value	Value	Value	Value	Value	Value	Value	Value	Value	Value	Value	Value	Value	Value	Value	Value	Value
Value	Value	Value	Value	Value	Value	Value	Value	Value	Value	Value	Value	Value	Value	Value	Value	Value	Value	Value	Value	Value

Figure 2.12: Model of the final matrix 3054x21 obtained at the end of the data extraction process for each parameters combination.

2.4 Data analysis and results

After the data extraction, the next step is a data analysis using MATLAB Software in order to demonstrate the accuracy of FE analysis results and the congruence with the theoretical ones.

First of all, an importation of the previous '.txt' result files from the specific Ansys working directory into MATLAB Software is implemented. Analysis elements of interest are:
- Beam nodes: with a node ID from 1 to 2916
- Nodule nodes: with a node ID from 2917 to 3054
- Nodes of the base area of the nodule: with a node ID from 2933 to 2944, in order to calculate the nodule reaction force

A rearrangement of results matrices is proposed to allow a direct discrimination of the nodes membership (beam node/nodule node) attributing the value '1' to beam's nodes and the value '3'

to nodule's nodes. Therefore, a further matrix column, containing only the values 1 or 3, is proposed in addition to the previous ones.

Moreover, the reaction force on the nodule (Fz) -expressed in Newton (N)- is obtained for each parameters combination and a further matrix column, containing the reaction force value, is added to the previous ones. First of all, the average SZ is obtained adding the stress along z (SZ) on the 12 nodes belonging to the base area of the nodule (with a node ID from 2933 to 2944) and then dividing for the number of nodes. The reaction force for the parameters combination is obtained by multiplying the average SZ with the base area of the nodule. As a consequence, a negative value of the nodule reaction force is expected.

The final rearrangement step is a conversion of the previous '.txt' results' file format into a '.mat' format, to facilitate the data plotting and manipulation.

A model of the final matrix 3054x23, saved in a '.mat' file, obtained at the end of the data rearrangement process for each parameters' combination is presented below in Figure 2.13:

P1	P2	P3	NODE #	X NODE	Y NODE	Z NODE	EPTO EQV	EPTO X	EPTO Y	EPTO Z	EPTO XY	EPTO YZ	EPTO XZ	SEQV	SX	SY	SZ	SXY	SYZ	SXZ	Fz	1/3
Value	Value	Value	Value	Value	Value	Value	Value	Value	Value	Value	Value	Value	Value	Value	Value	Val	Val	Value	Value	Value	Value	Value
Value	Value	Value	Value	Value	Value	Value	Value	Value	Value	Value	Value	Value	Value	Value	Value	Val	Val	Value	Value	Value	Value	Value
Value	Value	Value	Value	Value	Value	Value	Value	Value	Value	Value	Value	Value	Value	Value	Value	Val	Val	Value	Value	Value	Value	Value
Value	Value	Value	Value	Value	Value	Value	Value	Value	Value	Value	Value	Value	Value	Value	Value	Val	Val	Value	Value	Value	Value	Value

Figure 2.13: Model of the final matrix 3054x23 obtained at the end of the data rearrangement process for each parameters combination.

Consequently, a plot of some results of interest is performed to validate the FE results. In particular, the plotted results are referred to all nodes of the six layers along the z axis of the mesh separately. Therefore, there are six different plotted graphs -one for each beam's mesh layer along z axis- for each input parameters combination and for each result of interest. Beam mesh layers along z axis (named with the 'h' variable) range from h=0 mm to h=2 mm with a step of 0.4 mm, covering the entire thickness of the beam. A plot of the nodes composing the entire mesh, with the layers along the beam thickness, is proposed in Figure 2.14:
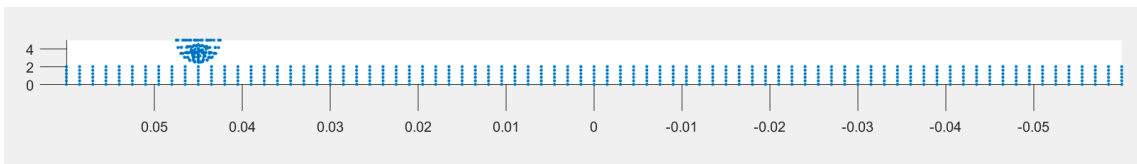

Figure 2.14: Beam mesh layers along z axis (named with the 'h' variable) range from h=0 mm to h=2 mm with a step of 0.4 mm, covering the entire thickness of the beam.

Plotted results for each input parameters combination are:
• Total von Mises mechanical strain (EPTOEQV), for each layer of the beam mesh along the z axis (column number 8 of the results matrix).
• Strain along the z axis (EPTOZ), for each layer of the beam mesh along the z axis (column number 11 of the results matrix).
• Total von Mises mechanical stress (SEQV), for each layer of the beam mesh along the z axis (column number 15 of the results matrix).
• Stress along the z axis (SZ), for each layer of the beam mesh along the z axis (column number 18 of the results matrix).
There are 1331 different combinations of input parameters, 4 results of interest need to be plotted (EPTOEQV, EPTOZ, SEQV, SZ) for each layer of the beam mesh along the z axis (6 layers) for a total number of plotted graphs of 31944. Different plotted graphs are directly saved in a 'png' format in four especially dedicated directory based on the result of interest to allow a better visualization and search.

Some significant graphs for each result of interest and for different layers are exposed in the following Figures. In each plotted graph is highlighted the corresponding input parameter combination, the 'h' value, the obtained value of nodule reaction force (Fz), the fingertip centre position along the tool major axis (y_central input parameter) in red and the hemisphere centre position along the tool major axis (y_hemisphere input parameter) in blue.

1) Total von Mises mechanical strain (EPTOEQV) plotted graphs for the 'h' value of 1.6 mm (Figure 2.15):
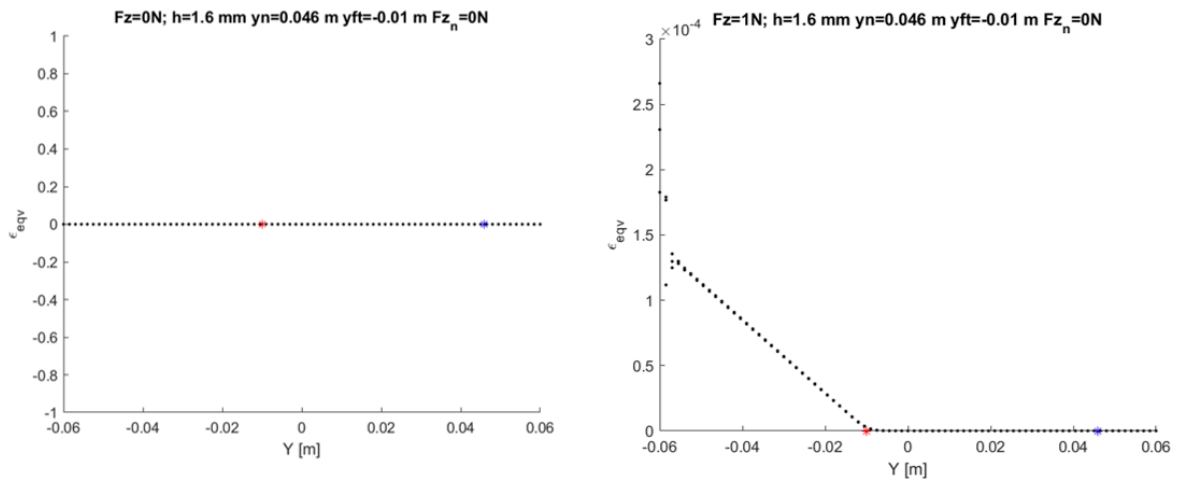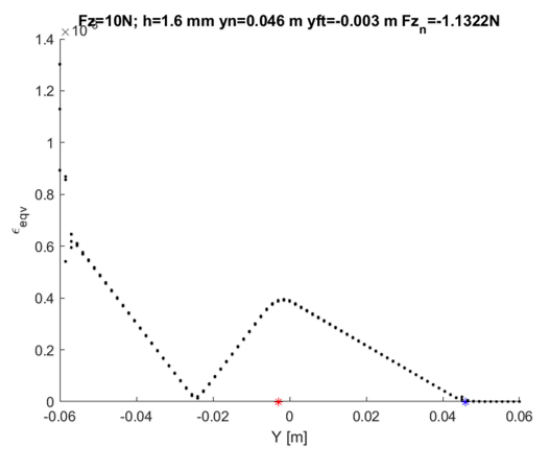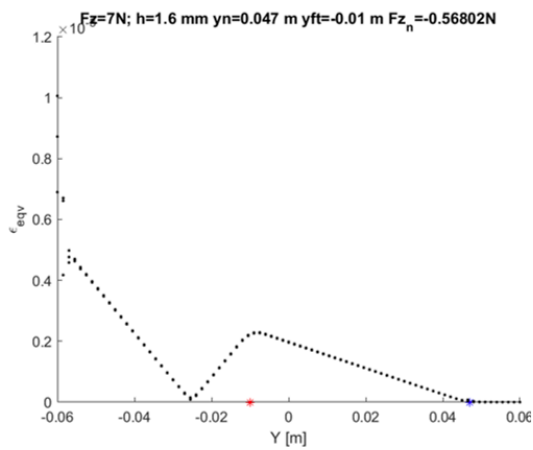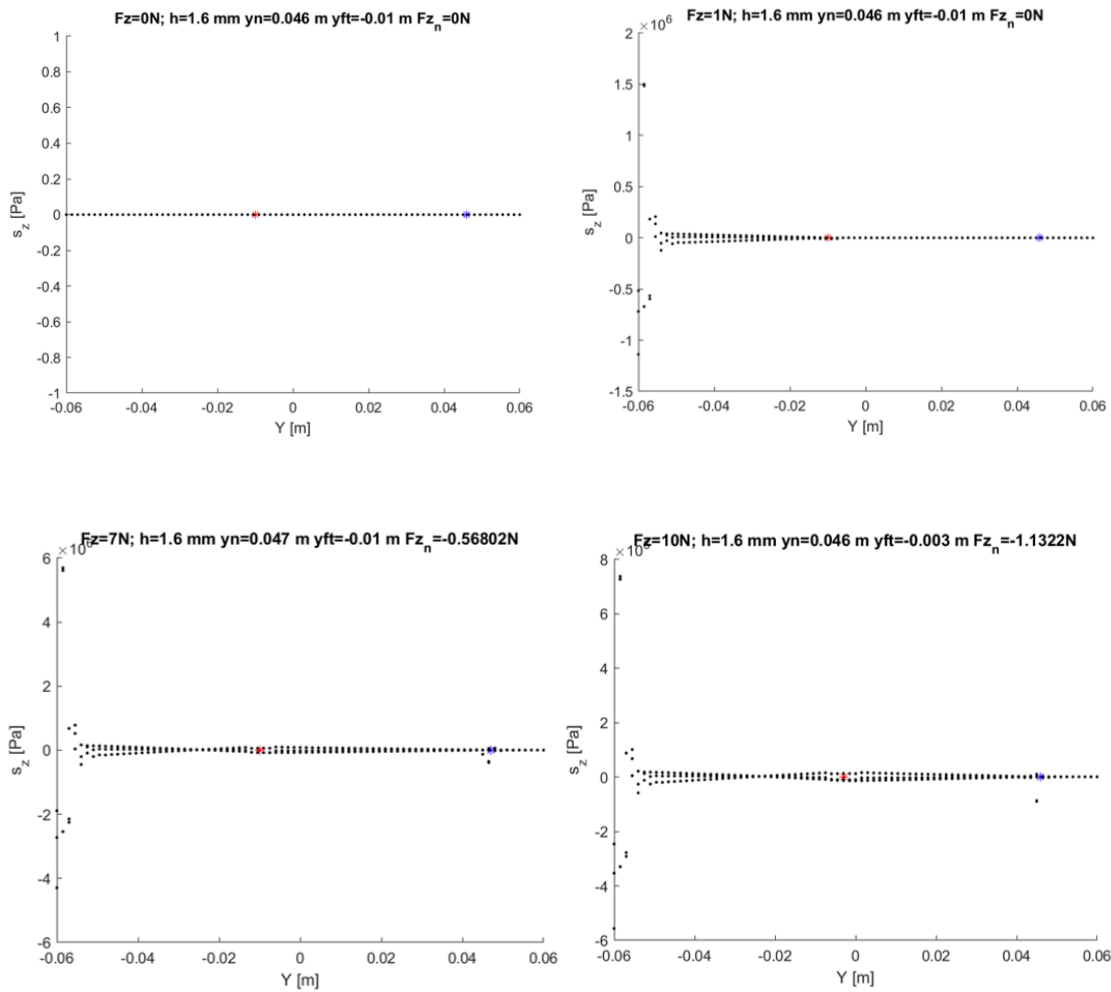
2) Strain along the z axis (EPTOZ) plotted graphs for the 'h' value of 1.6 mm (Figure 2.16):
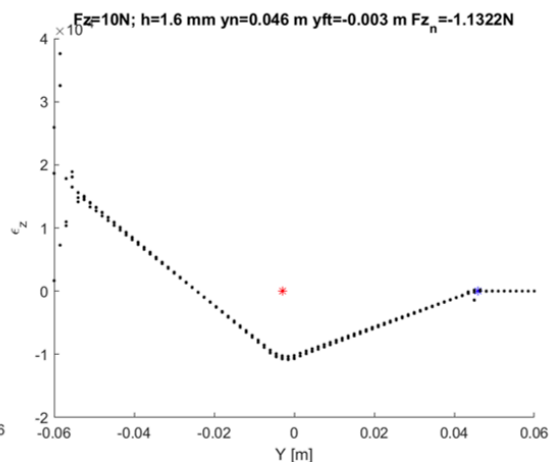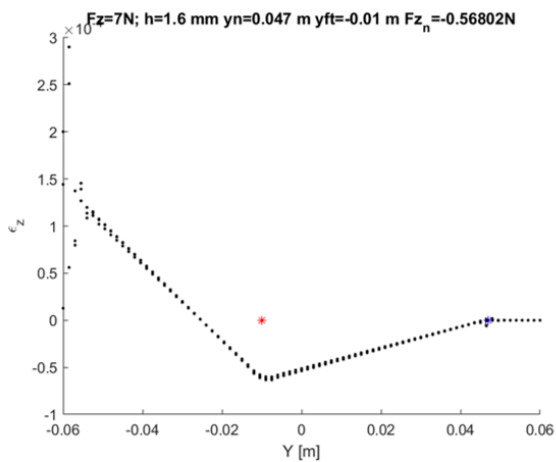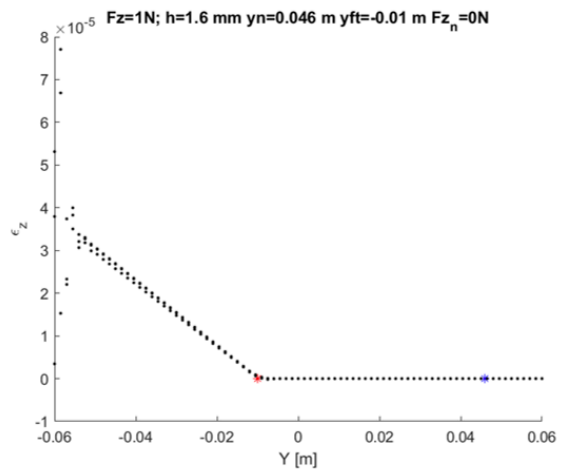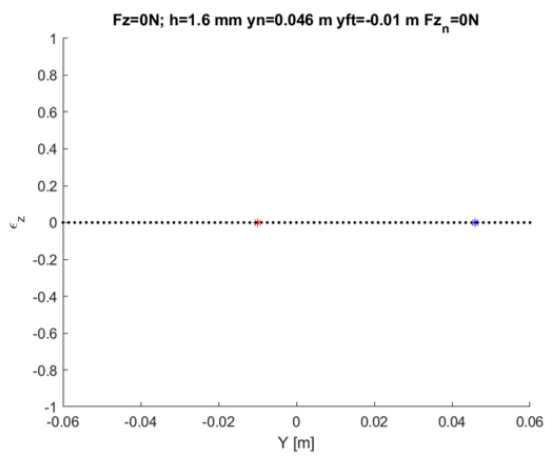
(3) Total von Mises mechanical stress (SEQV) plotted graphs for the 'h' value of 1.6 mm (Figure 2.17):
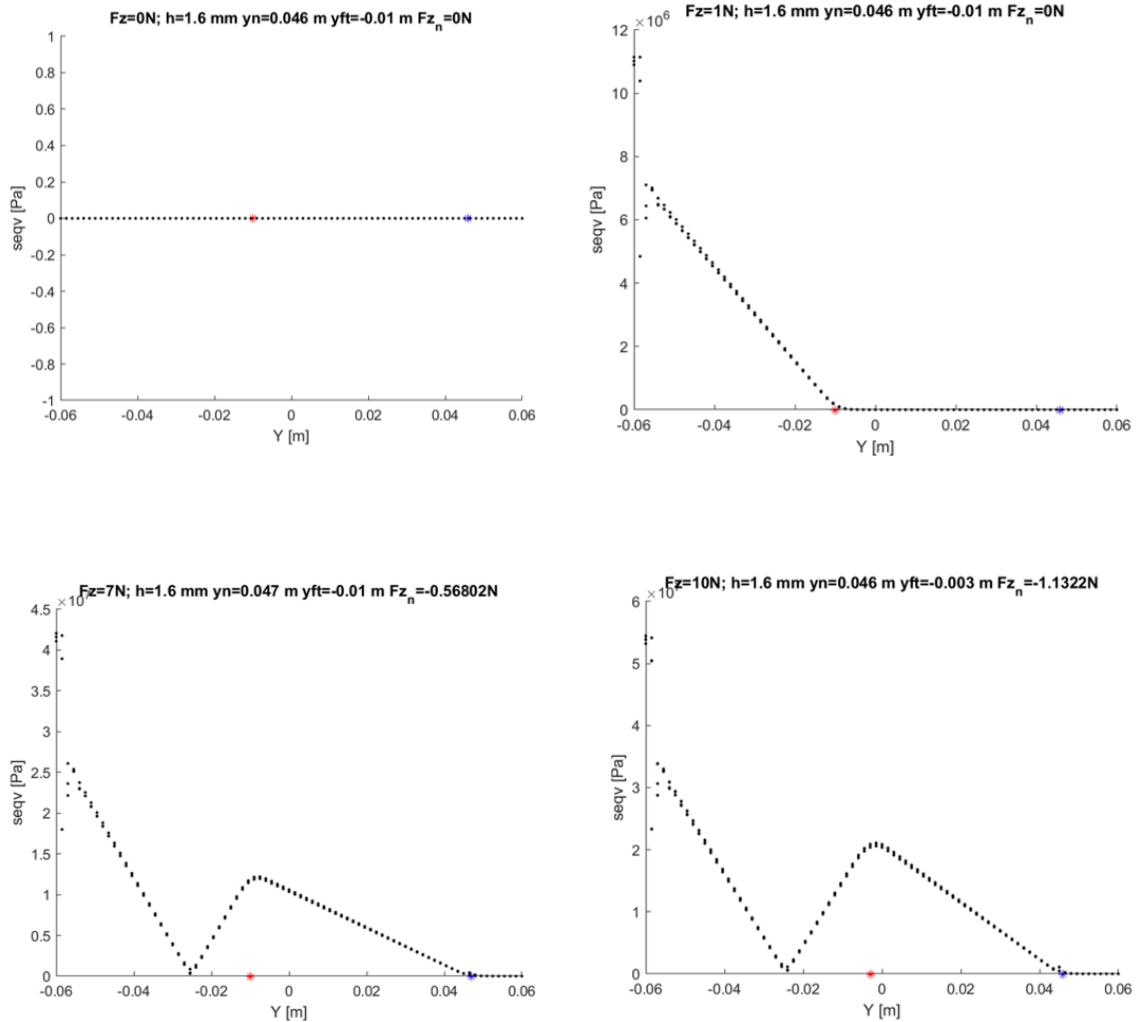
4) Stress along the z axis (SZ) plotted graphs for the 'h' value of 1.6 mm (Figure 2.18):

Fz=0N; h=1.6 mm yn=0.046 m yft=-0.01 m Fz_n=0N

Fz=1N; h=1.6 mm yn=0.046 m yft=-0.01 m Fz_n=0N

Fz=7N; h=1.6 mm yn=0.047 m yft=-0.01 m Fz_n=-0.56802N

Fz=10N; h=1.6 mm yn=0.046 m yft=-0.003 m Fz_n=-1.1322N

2.5 FBGs optimization via Neural Networks, Neural Networks input and output

In this Section the implementation of ad hoc Neural Networks using MATLAB software will be discuss with a dual aim:

• To demonstrate the feasibility of FE simulation input parameters reconstruction (y_central input parameter, y_hemisphere input parameter, handle_load_intensity input parameter) and nodule reaction force (Fz) starting from the corresponding EPTOY value on the beam nodes (the column number '10' of results matrices).

• To obtain the best FBGs-based sensors positioning along the beam with an automatized method, maximizing the neural network performance. Each node of the beam (Node ID from 1 to 2916) could be a candidate for the FBG positioning.

The choice to employ optical FBGs-based sensors is due to the unique properties of optical sensors, essential in biomedical applications, such as biocompatibility, chemical inertness, immunity to electromagnetic interferences and high sensitivity. Main limits include susceptibility to temperature, relatively high cost, complex information processing system and size limitations. As a consequence, their employment in biomedical applications is rapidly increasing. Optical sensors,

including optical fiber and FBGs sensors, obtain tactile information by analysing wavelength changes. FBGs sensors detect force and moment information using the variation in the FBG reflection spectrum induced by the applied load to be measure.

In this work, FBGs-based sensors are employed to detect the strain along a single direction.

The basic concept is to find out the optimum positioning of six FBGs sensing elements, browsing through each of the 2916 mesh nodes composing the beam. The use of six FBGs sensing elements could be an adequate compromise between detection capability, design complexity and cost. Therefore, the process is leaded to a 6 nodes position choice, each representing the position of 6 FBGs elements.

The reference dataset is composed by the 1331 '.mat' file results (each file results is a matrix 3054x23) obtained at the end of the data rearrangement process exposed in the paragraph 2.4 and saved in a specific directory.

Two different FBGs configurations are considered in this process:

1) A horseshoe FBGs configuration, employing six FBGs sensors disposed on the same thickness plane (using as a reference the nodes z-coordinate) in a specular way in relation to the same central axis. In other words, the following conditions must be respected during the node scanning:

training_node_1=[-x_node -y_node z_node]
training_node_2=[-x_node y_node z_node]
training_node_3=[-x_node 0 z_node]
training_node_4=[x_node 0 z_node]
training_node_5=[x_node -y_node z_node]
training_node_6=[x_node y_node z_node]

2) A random FBGs configuration, employing six FBGs sensors without any constrain in terms of positioning and nodes coordinates. The combinations of six nodes are chosen randomly in the Node ID range 1-2916. This configuration is essential to extract the best neural network performance in terms of Mean Squared Error in order to compare the horseshoe configuration value with the random configuration value.

Moreover, the implementation of a tolerance-based algorithm (tolerance equal to 10^{-10}) is necessary to match the Nodes ID with the nodes coordinates along the x-/y-/z- axis, because of the numerical approximations of results due to the FE analysis.

The results matrix column of interest is the column number '10', related to the strain value along the y axis (EPTOY) of the beam's nodes, since this is the result of interest we would like to detect with the FBGs-based sensors. A further strength of the proposed method is the flexibility in changing the column of interest related to a specific result of interest, keeping unchanged the procedure.

Input and output of the Neural Network (NN):
• _NN Input: A 6x1331 matrix, with a number of rows corresponding to six training nodes and a number of columns equal to the number of results files of the dataset (Figure 2.19). Each matrix element contains the EPTOY value for the training node in question for each results file of the dataset. In this way all the EPTOY values related to each combination of FE analysis input parameter are considered.

	1	2	3	4	...	1331
Training_node_1	EPTOY (i, j)	EPTOY (i, j)	EPTOY (i, j)	EPTOY (i, j)	...	EPTOY (i, j)
Training_node_2	EPTOY (i, j)	EPTOY (i, j)	EPTOY (i, j)	EPTOY (i, j)	...	EPTOY (i, j)
Training_node_3	EPTOY (i, j)	EPTOY (i, j)	EPTOY (i, j)	EPTOY (i, j)	...	EPTOY (i, j)
Training_node_4	EPTOY (i, j)	EPTOY (i, j)	EPTOY (i, j)	EPTOY (i, j)	...	EPTOY (i, j)
Training_node_5	EPTOY (i, j)	EPTOY (i, j)	EPTOY (i, j)	EPTOY (i, j)	...	EPTOY (i, j)
Training_node_6	EPTOY (i, j)	EPTOY (i, j)	EPTOY (i, j)	EPTOY (i, j)	...	EPTOY (i, j)

Figure 2.19: Input matrix (6x1331) of the Neural Network.

• NN Output: A 4x1331 matrix, with a number of rows corresponding to the number of the input parameters in the FE Analysis (y_hemisphere, y_central, handle_load_intensity) and a fourth row corresponding to the nodule reaction force. The number of columns is equal to the number of results files of the dataset (Figure 2.20).
The first/second/third/fourth row elements consist of the y_hemisphere/y_central /handle_load_intensity values respectively, originating the corresponding EPTOY values in the training nodes of the input matrix.

	1	2	3	4	...	1331
y_hemisphere	Value	Value	Value	Value	...	Value
y_central	Value	Value	Value	Value	...	Value
handle_load_intensity	Value	Value	Value	Value	...	Value
nodule_reaction_force	Value	Value	Value	Value	...	Value

Figure 2.20: Output matrix (4x1331) of the neural network.

The final aim of this artificial intelligence method is the obtaining of a 2916x7 matrix, called nodes_errors_matrix. The number of matrix rows correspond to the total number of nodes considered in each combination of possible FBGs positions. The number of columns correspond to the number of the six candidates Nodes ID for FBGs positioning and the neural network performance related to the nodes combination (Figure 2.21). Each row of the matrix is obtained after a Neural Network training; thus 2916 different NN training phases are necessary to compose the final nodes_errors_matrix. In the end, only the six Nodes ID related to the best NN performance in terms of NN Mean Squared Error will be elected for the six FBGs final positioning.

	Node ID 1	Node ID 2	Node ID 3	Node ID 4	Node ID 5	Node ID 6	NN performance
1	Value	Value	Value	Value	Value	Value	Value
2	Value	Value	Value	Value	Value	Value	Value
3	Value	Value	Value	Value	Value	Value	Value
4	Value	Value	Value	Value	Value	Value	Value
.	.	.	.	.	.	.	.
.	.	.	.	.	.	.	.
.	.	.	.	.	.	.	.
2916	Value	Value	Value	Value	Value	Value	Value

Figure 2.21: Nodes_errors_matrix (2916x6), containing all the candidate combinations of nodes for the 6 FBGs positioning and the relative NN performance.

2.6 Neural Networks architecture and training

The Neural Network implementation and training are carried on with the MATLAB Neural Network Start 'nnstart' tool for Input-Output and curve fitting.
The entire starting dataset consisting of 1331 '.mat' result files (each result matrix is a 3054x23 matrix) can be subdivided into three sub-categories:
• _Training set: dataset for the Neural Network training, composed by 905 result files (training ratio equal to 0.68). These samples are presented to the network during training, and the network is adjusted according to its error.
• _Validation set: dataset for the Neural Network validation process, composed by 213 result files (validation ratio equal to 0.16). These samples are used to measure network generalization, and to halt training when generalization stops improving.
• _Testing set: dataset for the Neural Network testing process, composed by 213 result files (validation ratio equal to 0.16).

The dataset partition into the three sub-categories is totally random with the only ratios defined.
The proposed Neural Network is a two-layer feed-forward network able to fit multi-dimensional mapping problems (Figure 2.22).
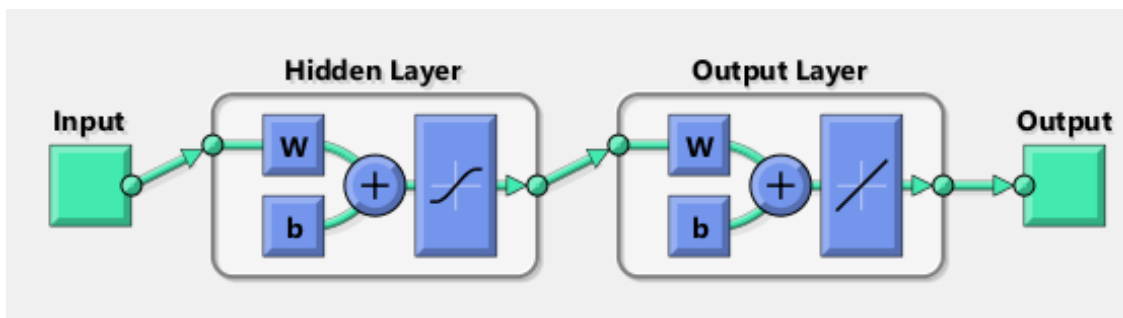
The number of NN hidden layers is fixed to '10'.

• _The chosen NN training algorithm is the Levenberg-Marquardt algorithm, that requires more memory but less time. Training automatically stops when generalization stops improving

• _The NN performance is evaluated in terms of Mean Squared Error (MSE) and Regression (R). MSE is the average squared difference between outputs and targets. Lower values are better (zero means no error). Regression values measure the correlation between outputs and targets. An R value of 1 means a close relationship.

The NN regression plots, related to the errors_nodes_matrix, are displayed in Figure 2.23. The R parameter is extremely close to the value of 1, showing the training goodness.
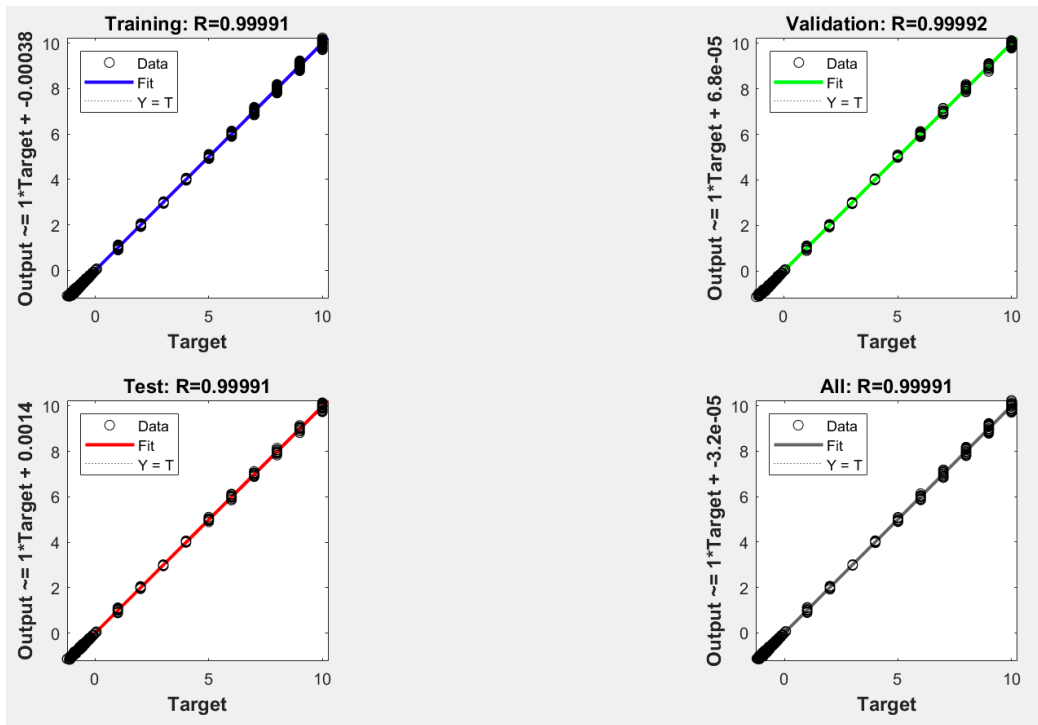
2.7 Neural Networks implementation and FBGs sensing elements positioning

The previous Neural Network is implemented in four different working conditions:

To find out the best horseshoe 6-FBGs configuration in ideal conditions, without any measurement noise. Six FBGs sensing elements disposed on the same thickness plane (using as a reference the nodes z-coordinate) in a specular way in relation to the same central axis. In other words, the following conditions must be respected during the node scanning:

training_node_1=[-x_node -y_node z_node]
training_node_2=[-x_node y_node z_node]
training_node_3=[-x_node 0 z_node]
training_node_4=[x_node 0 z_node]

training_node_5=[x_node -y_node z_node]
training_node_6=[x_node y_node z_node]

After 2916 Neural Networks trainings, the process will return a 2916x7 matrix, called nodes_errors_matrix. The number of matrix's rows correspond to the total number of nodes considered in each combination of possible FBGs positions. The number of columns correspond to the number of the six candidates Nodes ID for FBGs positioning and the neural network performance related to the nodes' combination (Figure 3.3). Each row of the matrix is obtained after a neural network training; thus 2916 different NN training phases are necessary to compose the final nodes_errors_matrix. In the end, only the six Nodes ID related to the best NN performance in terms of NN Mean Squared Error (MSE) will be elected for the six FBGs final positioning (Figure 2.24). Minimum MSE means the best NN performance.
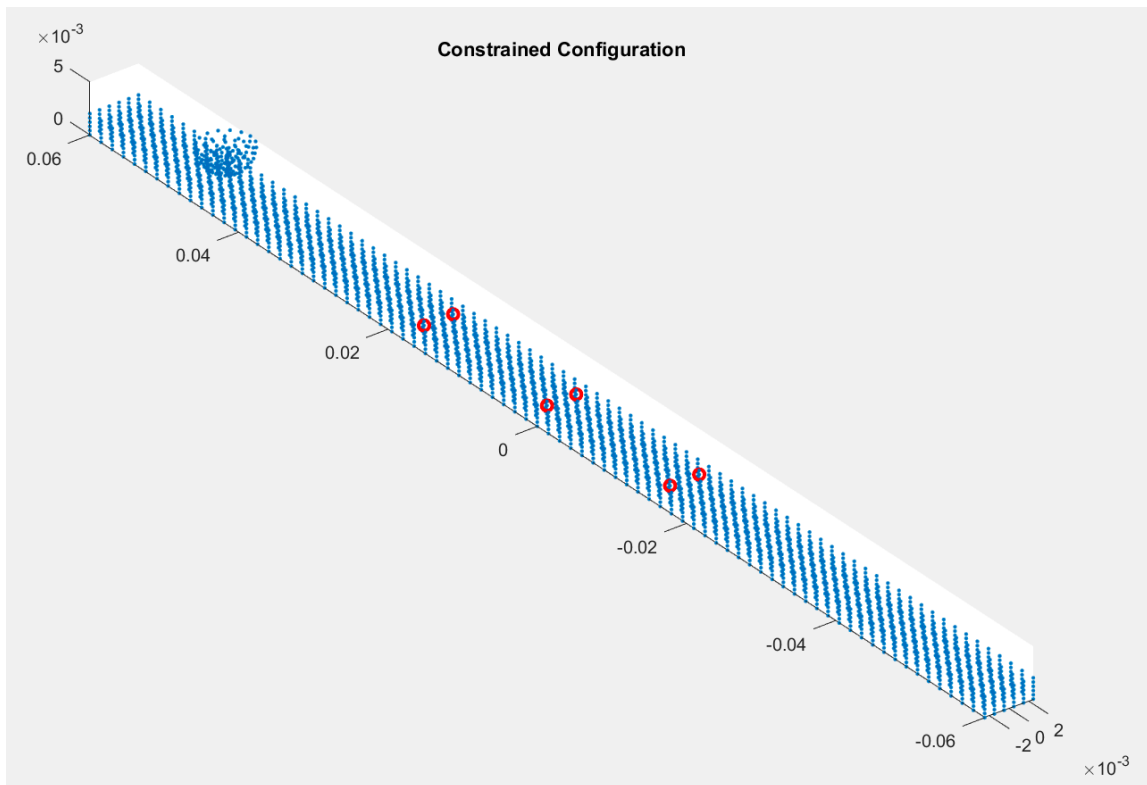
Figure 2.24: Final FBGs positioning for the horseshoe 6-FBGs configuration in ideal conditions, without any measurement noise.

2) To find out the best random 6-FBGs configuration in ideal conditions, without any measurement noise. Six FBGs sensing elements, without any constrain in terms of positioning and nodes coordinates, can be selected. The combinations of six nodes are chosen randomly in the Node ID range 1-2916. This configuration is essential to extract the best neural network performance in terms MSE in order to compare the horseshoe configuration value with the random configuration value.

After 2916 Neural Networks trainings, the process will return a 2916x7 matrix, called nodes_errors_random_matrix. Each row of the matrix is obtained after a neural network training; thus 2916 different NN training phases are necessary to compose the final nodes_errors_random_matrix. In the end, only the six Nodes ID related to the best NN performance in terms of NN Mean Squared Error (MSE) will be elected for the six FBGs final positioning (Figure 2.25). This is the best working condition in terms of performance.
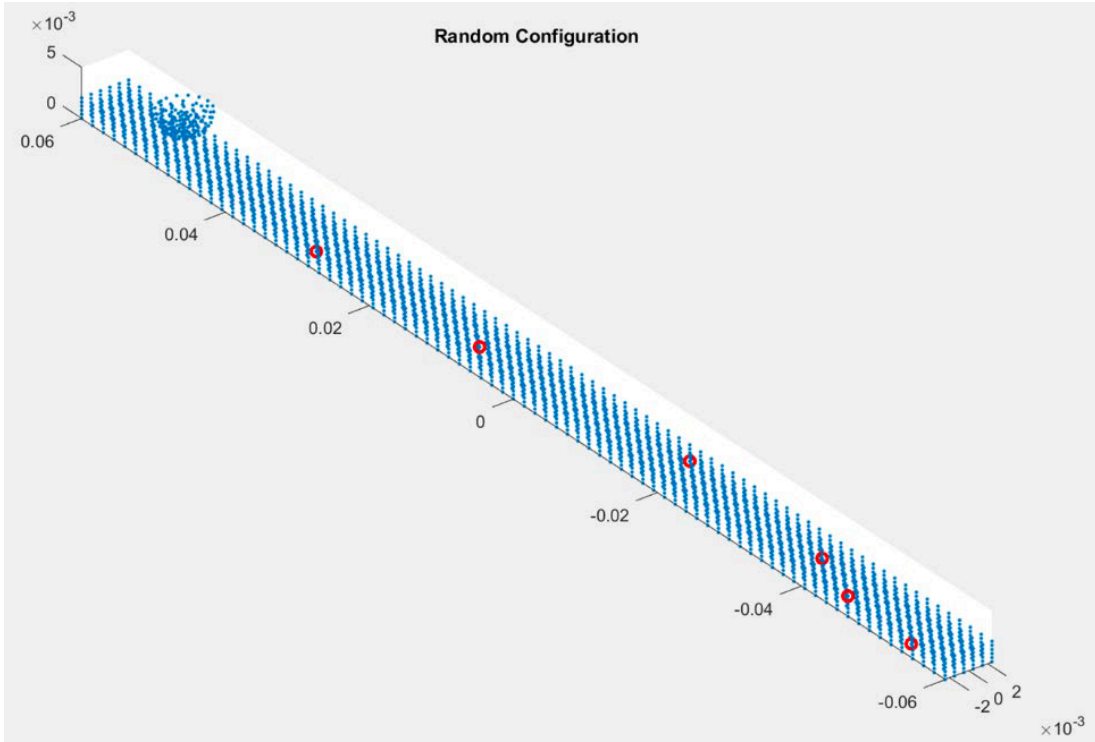
Figure 2.25: Final FBGs positioning for the random 6-FBGs configuration in ideal conditions, without any measurement noise.

3) To find out the best horseshoe 6-FBGs configuration in real conditions, with a measurement noise. The input NN data (EPTOY results composing the input matrix) present a gaussian noise (a Gaussian probability distribution with average equal to zero). Therefore, there will be values of strain along the y axis (EPTOY) equal to the sum of the value of strain along the y axis in ideal conditions with the 3% of the maximum EPTOY obtained in all the combinations.

After 2916 Neural Networks trainings, the process will return a 2916x7 matrix, called nodes_errors_gaussian_matrix. In the end, only the six Nodes ID related to the best NN performance in terms of NN Mean Squared Error (MSE) will be elected for the six FBGs final positioning.

4) To find out the best random 6-FBGs configuration in real conditions, with a measurement noise. The input NN data (EPTOY results composing the input matrix) present a gaussian noise (a Gaussian probability distribution with average equal to zero). Therefore, there will be values of strain along the y axis (EPTOY) equal to the sum of the value of strain along the y axis in ideal conditions with the 3% of the maximum EPTOY obtained in all the combinations.

After 2916 Neural Networks trainings, the process will return a 2916x7 matrix, called nodes_errors_random_gaussian_matrix. In the end, only the six Nodes ID related to the best NN performance in terms of NN Mean Squared Error (MSE) will be elected for the six FBGs final positioning. This is the worst working condition in terms of performance because of the coincidence of measurement noise and random 6-FBGs configuration.
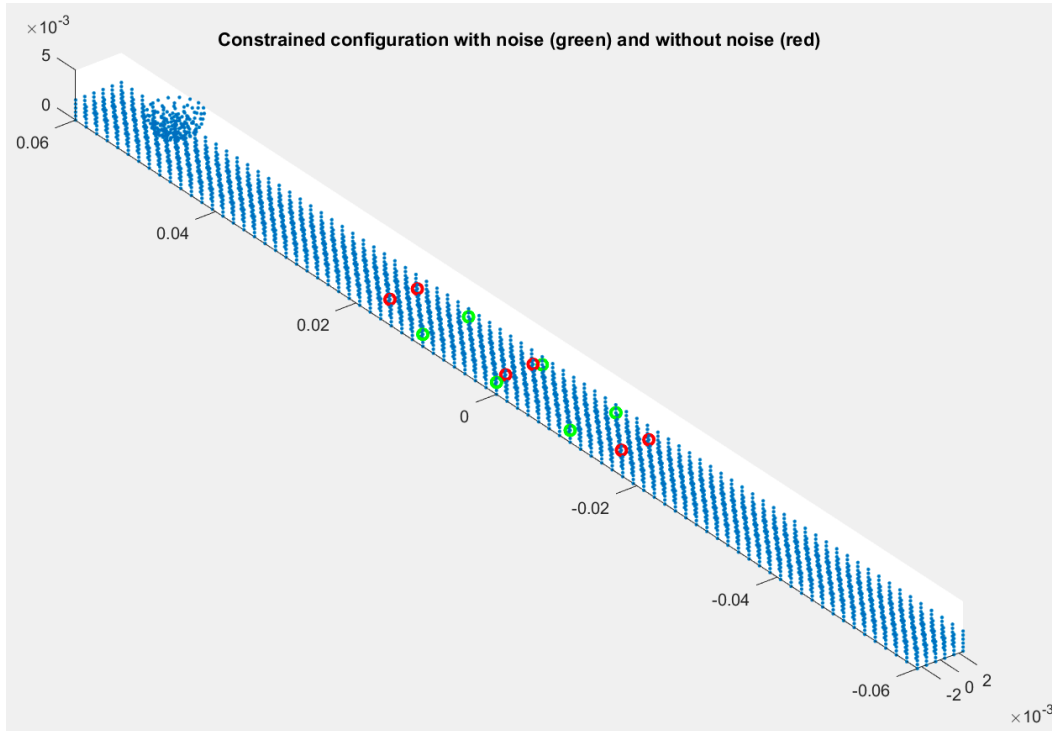

Figure 2.26: Final FBGs positioning for the horseshoe 6-FBGs configuration in ideal conditions (in red) and real conditions (in green).

2.8 Neural Networks performance and final FBGs sensing elements positioning choice

Making a comparison among the four final different 6-FBGs configurations, discussed in Section 2.7, some issues should be taken in consideration. First of all, the different best performance of the Neural Network, investigating the beam's nodes, in the four working conditions. The best NN performance, in terms of MSE (lower values are better, zero means no error), can be identified in the seventh column of the errors-nodes-matrix obtained in the end the training process. The MSE is marked for each 6-nodes combination, investigated by the NN.

A summary of the best NN performances in terms of MSE, for the four different working conditions, is noted in Figure 2.27:

	CONSTRAINED CONFIGURATION	**RANDOM CONFIGURATION**
IDEAL CONDITIONS	$2.2596 * 10^{-5}$	$5.89 * 10^{-7}$
REAL CONDITIONS	0.0016	0.0066

The best NN performance can be noticed obviously in the NN ideal working conditions, without any measurement noise, with a random nodes choice probably because of the constraints' absence during the investigation. This result can be considered as a landmark for the other working conditions. However, the two final 6-FBGs positions with a constrained horseshoe configuration allow a better mechanical design due to the symmetry and a greater manufacturability using additive manufacturing methods, without clear deviations in NN performance. Thus, the choice fell on this configuration type. Regarding the constrained configuration in ideal conditions a NN performance value close to the reference one (random configuration) is obtained.

Moreover, despite of the appreciable difference between ideal conditions and real conditions in the horseshoe configuration (Figure 3.8), in both cases the six-FBGs positioning falls back into the beam's middle section within a range of -20 mm to +20 mm around the zero value along the major beam y axis. Regarding the z coordinate, both results are very close: the ideal conditions one at a z- axis value of 1.6 mm while the real conditions at a z-axis value of 1.2 mm (Figure 2.28).
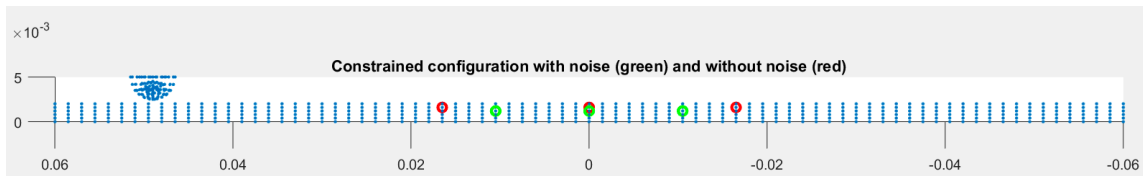
Definitely, in light of the previous considerations, the final 6-FBGs positioning choice falls on the constrained configuration in ideal conditions with the associated following Nodes ID:
The final Nodes ID for 6-FBGs positioning are [2456, 2104, 2280, 2292, 2468, 2116] corresponding to the nodes in red in Figure 2.26/Figure 2.28.

2.9 Constructive requests and instrument design rearrangement

The next milestone of the work includes a rearrangement of the design tools previously described, both for the FE analysis and the machine learning algorithms. This is a necessary stage to match the previous simulation issues and results with the constructive requests in terms of fabrication feasibility. This is the step preceding the 3D printing device realization and the FBGs-based optical sensors fabrication.

The Aluminium beam frame realization occurs at the Certema S.c.a.r.l. "Laboratorio Tecnologico Di Grosseto (GR)", thanks to a partnership with the Scuola Superiore Sant'Anna of Pisa, while the FBGs based sensors achievement occurs at TeCIP Institute of the Scuola Superiore Sant'Anna.

Therefore, some regards have been made taking into account the Certema technological requests and available equipment as well as the TeCIP Institute optical sensors availability. A re-adaptation of the geometric frame design to allow an adequate sensors positioning, of the FE simulation parameters and of the NN dataset are necessary. Particularly:

Geometric design adjustment: two through holes have to cross along the metallic frame in positions identified at the end of the artificial intelligence process described in Chapter 2. These holes should host two optical fibers with the 6-FBGs sensing elements placed in particular beam points, thus the holes diameter should be major of the Coating optical fiber diameter in addition to a tolerance necessary for the frame-fibers gluing. The optical fibers available at TeCIP Institute have a Coating Diameter of 160 μm, thanks to the coating material employed (Polyimide). According to previous considerations, the two through holes will have a diameter of 300 μm.

Moreover, a housing is necessary to allow the beam fixing to moving plate of the experimental Set-Up machinery, using two M3 screws. Housing and beam are considered as a unique body, with a similar 'T' letter geometry (Figure 2.29), starting from the design step and in all the subsequent phases. The two M3 screws holes should be considered in the FE analysis while the two through holes crossing the frame can be neglected because of the reduced dimensions in comparison with the beam's ones.
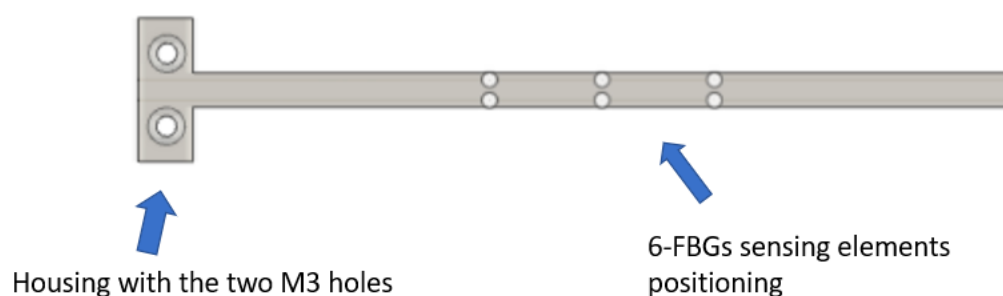

Housing with the two M3 holes

6-FBGs sensing elements positioning

Figure 2.29: Geometric design adjustment

2.10 Finite Elements analysis and Neural Networks rearrangement

Regarding the FE analysis of a nodule gripping procedure, some changes are necessary to meet the fabrication issues (FE simulation features not mentioned below remain unchanged in comparison with features described in Section 2.3):

1) Material Properties: the metallic frame is obtained with an additive manufacturing method using the Concept Laser M2 Cusing instrument and the CL 30AL Aluminium alloy. Hence, a change in the FE material property is necessary, according to the employed material datasheet, regarding the Young Module.

The CL 30AL Aluminium alloy has a Young Module of 75 GPa after the printing and a recommended heat treatment.

2) Model Realization: the two M3 screws holes should be considered in the FE analysis as well as the housing (the final body has a similar 'T' letter geometry) while the two through holes crossing the frame can be neglected because of the reduced dimensions in comparison with the beam's ones. The housing and the two M3 screws are performed directly in the Ansys Mechanical APDL environment using Boolean instructions. To allow a better meshing phase and nodes merging the housing is subdivided into two different parts: a part is called base_housing and it is directly in contact with the original beam and with the screws_housing (Figure 2.30)

Base_housing (in purple)
Screws_housing (in blue)
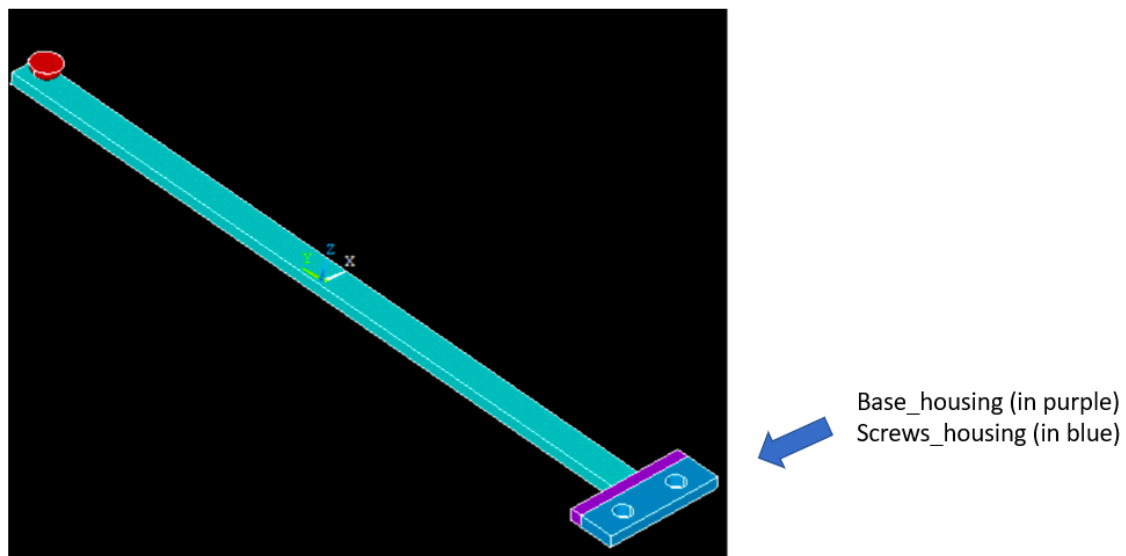
Meshing: A mapped mesh is implemented in the original beam and in the base_housing, while a free mesh is implemented in the hemisphere and in the screws_housing (

4) Implementation of mechanical contacts: This phase is initially performed with the Ansys APDL contact manager and subsequently with an ad hoc APDL code (see Appendix 2) for the automatization.

5) Mechanical constraints, mechanical loads: Two fixed structural constraints (x, y, z axes) are implemented inside the two screw holes to simulate a screwing constrain and to guarantee system's mechanical balance (Figure 2.31). Another fixed structural constraint (x, y, z axes) is implemented in the base area of the hemisphere. Constraints are implemented in mesh nodes. There are no changes in mechanical loads implementation.
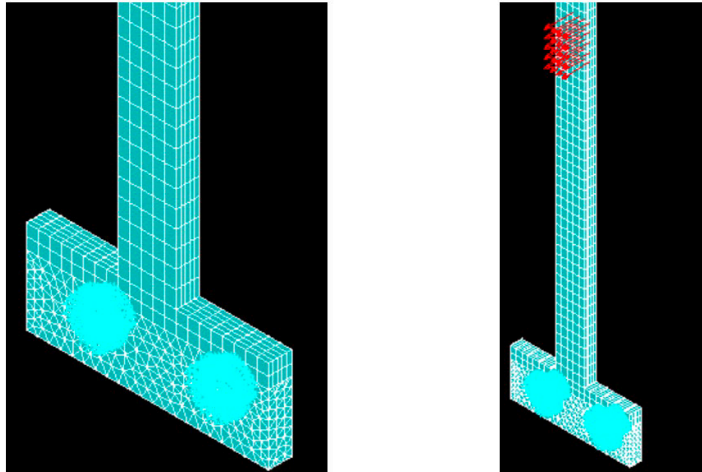
Qualitative results of total displacement, total von Mises mechanical strain and total von Mises mechanical stress are presented in (Figure 2.32)
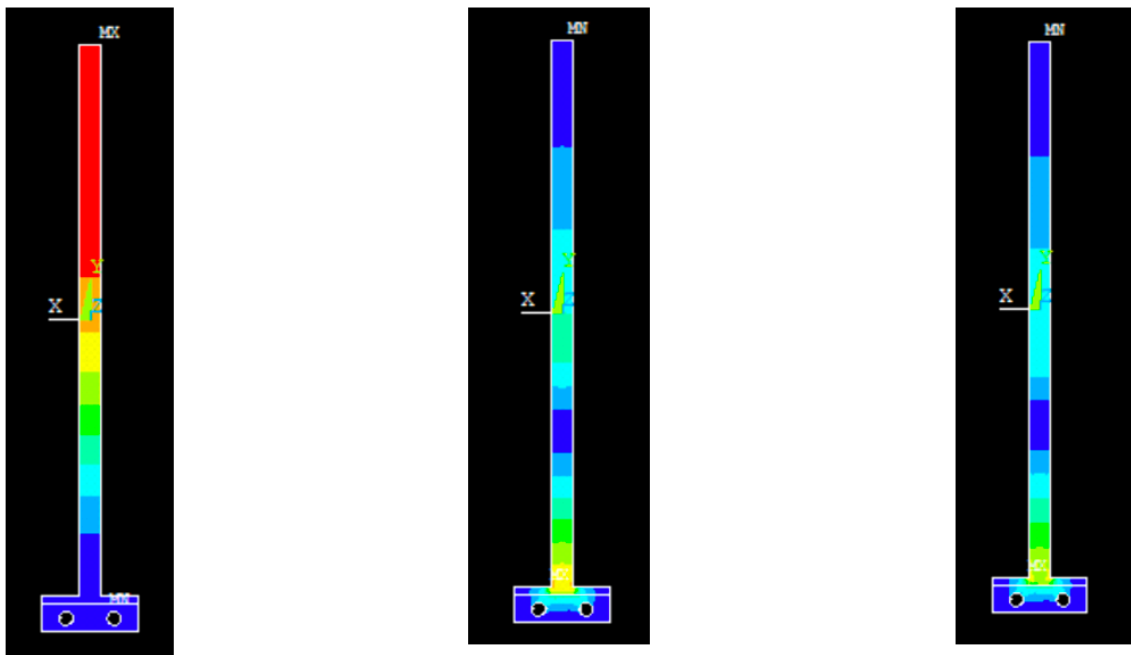

Figure 2.33: Qualitative simulation results for: (a) total displacement, (b) beam total mechanical von Mises strain for the input parameter combination Fingertip_force=7 N, nodule position along y_axis= -1 mm, fingertip position along y_axis=-9 mm, (c) beam total mechanical von Mises stress for the same parameters combination.

Qualitative results are very close to the previous results described in Section 2.3, with only some gaps in the housing location, because of the different mechanical constrains implementation. Subsequently, a quantitative analysis and an automatized data extraction are performed with Ansys Mechanical APDL Batch simulation environment. In particular, the extraction involves each node of the mesh for each combination of input parameters. Results of interest for each node of the mesh

are the same of Section 2.3. There are not differences in terms of data extraction and data analysis with the previous one, except for the higher number of nodes composing the housing-configuration mesh.

The next rearrangement phase is the NN process adaptation. In this case, only a few changes are necessary due to the different starting dataset. In particular, there is a different number of nodes composing the frame's mesh:

Nodes ID from 1 to 2916: nodes composing the original beam
Nodes ID from 2917 to 3054: nodes composing the nodule (hemisphere)
Nodes ID from 3055 to 3450: nodes composing the base_housing
Nodes ID from 3451 to 4636: nodes composing the base_housing

Only the Nodes ID from 1 to 2916 will be considered in the Neural Network investigation. In other words, only the original beam nodes are nominated for the 6-FBGs positioning.

Moreover, in light of the previous dissertations, the Neural Network is implemented only in the constrained horseshoe configuration for the ideal conditions (without any measurement noise) with an additional simplification: the NN investigation involves only the nodes y coordinate considering the z coordinate fixed to the value of 1.6 mm and the x coordinate fixed to the value of $1,5*10-3$, both obtained in the end of the process described in Section 2.8. This is an additional metallic frame's realization and geometry constraint.

Neural Network Input/Output are the same with a 6x1331 input matrix and a 4x1331 output matrix, as described in Section 3.1. The final aim of the process, after 81 Neural Networks trainings, is the achievement of an 81x7 matrix, called housing_nodes_errors_matrix. The number of matrix's rows correspond to the total number of layers along the beam's y axis. The number of columns correspond to the number of the six candidates Nodes ID for FBGs positioning and the neural network performance related to the nodes' combination. Each row of the matrix is obtained after a neural network training; thus 81 different NN training phases are necessary to compose the final housing_nodes_errors_matrix. In the end, only the six Nodes ID related to the best NN performance in terms of NN Mean Squared Error (MSE) will be elected for the six FBGs final positioning.

The best NN performance, compared with the previous performances, is displayed in Figure 2.33.

	CONSTRAINED CONFIGURATION	RANDOM CONFIGURATION	CONSTRAINED CONFIGURATION WITH HOUSING
IDEAL CONDITIONS	$2.2596*10^{-5}$	$5.89*10^{-7}$	$3.2955*10^{-5}$
REAL CONDITIONS	0.0016	0.0066	-

The extremely close performances under different NN working conditions demonstrate the accuracy in FE analysis combination of Input parameters reconstruction. As a consequence, the new 6-FBGs positioning results strictly near to the previous one.
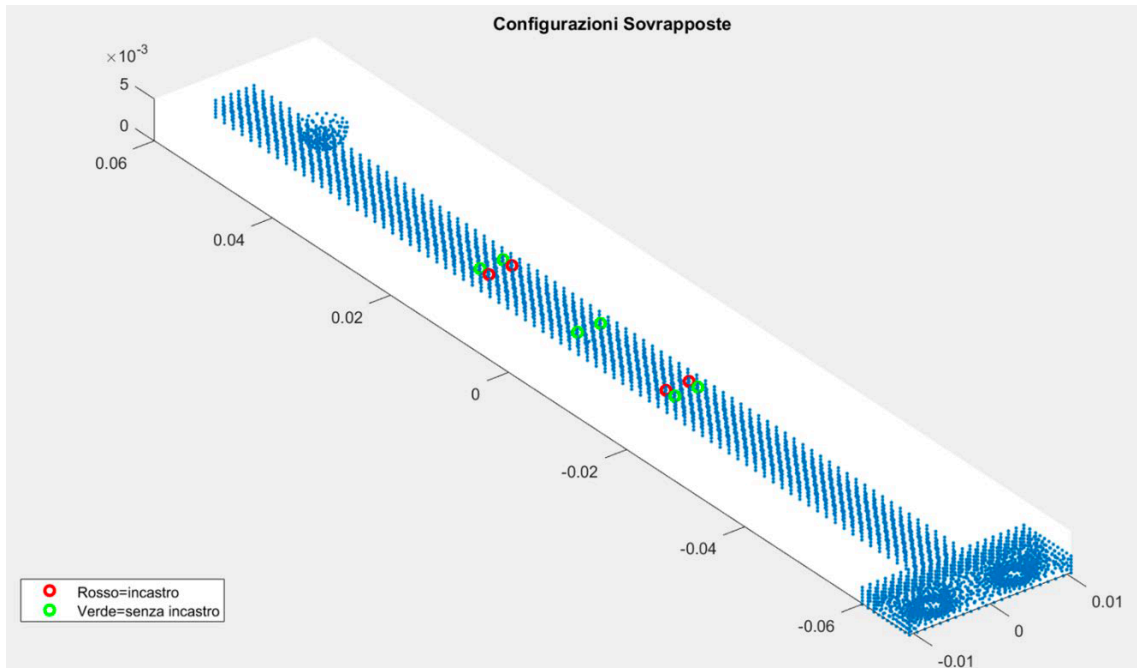
Figure 2.34: The final 6-FBGs sensing elements position (in red), in comparison with the previous one (in green.

3 Tool fabrication

3.1 Theoretical background and measurement principle of FBGs-based optical sensors

The structure of a general optical fiber is composed by an internal 'core' with a high refractive index and an external 'cladding' with a lower refractive index. The dissimilarity in terms of refractive index between core and cladding coerces the light into the core, allowing a refection at the interface.

In particular, the fiber Bragg grating (FBG) is a periodical variation of the core refractive index with a grating pitch (Λ). A FBG sensor is a sensing element embedded into the core of an optical fiber whose (24) main feature is the light reflection in a narrow band placed around the so-called Bragg wavelength ($\lambda\lambda BB$). When the light has a wavelength near to $\lambda\lambda BB$ there is a large amount of reflected light, and the structure resonates:

$$\lambda_B = 2Ne^{NNNN} * \Lambda$$

λ_B=Bragg wavelength
Ne^{NNNN}= effective reflective index

The FBG produces a reflected spectrum with a peak centred in the Bragg wavelength with a reflectivity included in a range 10%-90% in FBGs with a length from 3 mm to 10 mm. The reflected

bandwidth is approximately of 0.3 nm for FBGs wavelength of 1550 nm. In my thesis, six FBGs with previous features are employed (length of 3 mm, operating wavelength around 1550 nm).

The measurement principle of the FBGs is based on the dependence between $NNNNNNN$ and Λ, regarding strain and temperature. A strain along the fiber z-axis or a temperature variation induce a shift of the Bragg wavelength ($\nabla\lambda$) and consequently of the whole spectrum.

The FBGs-based optical sensors need dedicated connectors to link the fibers with a device, called optical interrogator (with a variable number of channels in the range 1-16), able to interrogate the FBGs sensing elements with a rapid scanning laser coupled to a photodetector (PD) followed by a transimpedance amplifier (TIA) coupled to a spectrometer (SP).
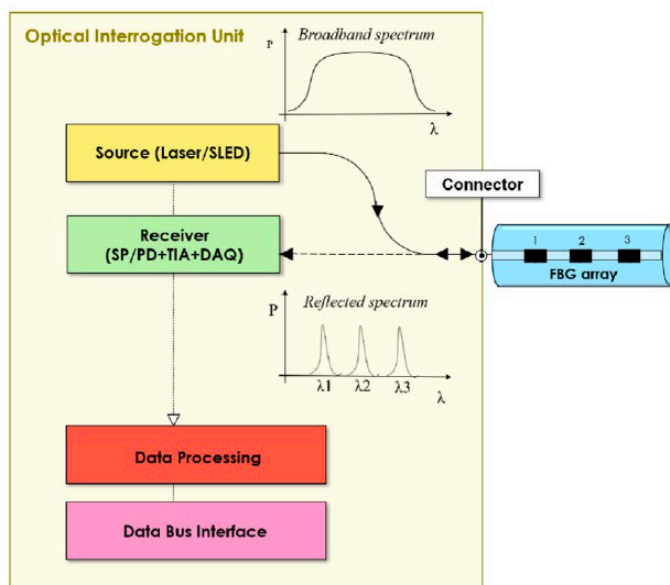
Figure 3.1: The entire schematic experimental Set-up to interrogate FBGs (24).
The FBGs-based sensors achievement occurs at the Institute of Mechanical Intelligence and Department of Excellence in Robotics & AI of Scuola Superiore Sant'Anna. The model design rearrangement is based on the equipment and optical fibers availability of the Institute. In particular, the choice falls on a germanium doped Single-Mode (SM) fiber model SM1250BI (9.8/125)P*, with a 9,8 µm core size and a 125 ± 1 µm cladding diameter, produced by the company FIBECORE. The fiber coating, realized in Polyimide, has a coating diameter of 155 ± 5 µm. Therefore, the two through holes crossing along the metallic frame should have a diameter of almost 300 µm to allow the fibers insertion and the following fibers gluing. Advantages of the employed fibers are bend insensitivity, hermetic coating and low loss. The full datasheet is proposed in Figure 3.2.

	SM1250BI (9.8/125)	SM1250BI (9.8/125)HT	SM1250BI (9.8/125)CHT	SM1250BI (9.8/125)P*	SM1250BI (9.8/125)CP
Operating Wavelength (nm)	1310 - 1650				
Cut-Off Wavelength (nm)	<1300				
Numerical Aperture	0.11 - 0.13				
Mode Field Diameter (μm)	9.0 - 10.6 @1550nm				
Attenuation (dB/km)	≤0.4 @1550nm				
Proof Test (%)	1 (100 kpsi)				
Cladding Diameter (μm)	125 ± 1		125 ± 2	125 ± 1	125 ± 2
Core Cladding Concentricity (μm)	<1.0				
Coating Diameter (μm)	245 ± 15			155 ± 5	
Coating Type	Dual Layer Acrylate	High Temperature Acrylate	Carbon and High Temperature Acrylate	Polyimide	Carbon and Polyimide
Operating Temperature (°C)	-55 to +85	-55 to +150		-50 to +300	

Figure 3.2: Optical fiber specifications.

Following the project specifications, the achievement of three equally spaced FBGs elements for each fiber is necessary. The chosen FBG length is 3 mm and each FBG is centred in the corresponding node of the frame mesh obtained in the previous Sections, at a distance from the tool's tip of 43.5 mm, 60 mm, 76.5 mm respectively as shown in Figure 3.3 (For the whole technical tables see Appendix 1).
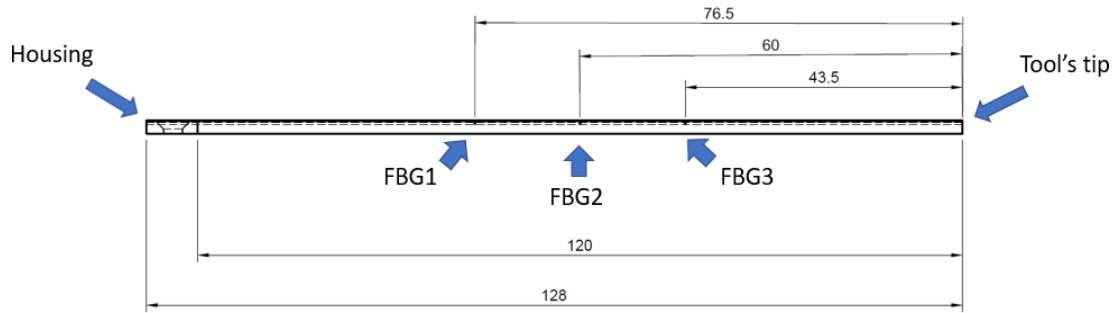
Figure 3.3: Positioning of the three FBGs elements along the fiber (lengths expressed in mm).
The two optical fibers with three FBGs embedded are specular, hence the following process can be implemented in the same way. The chosen reflection wavelengths for the three FBGs elements are respectively 1538 nm for FBG1 (the FBG closest to the housing), 1548 nm for FBG2 (the middle FBG) and 1558 nm for FBG3 (the FBG closest to the tip).
The 3 FBGs achievement process can be summarized in:

1) Fiber cleaning with Isopropyl alcohol to remove any impurities, able to modify the process.
2) Fiber manual alignment on the motorized vertical stage 8MVT120-25 (designed by 'standa' company). The alignment involves the x-y plane as well as the z-axis.

3) The laser beam is centred on the core fiber in the pre-established point in order to enable the FBG element (Figure 3.4). The laser machinery is produced by Newport company.

Figure 3.4: Laser beam centred in the core fiber, ready to work.

4) Setting of the energy profile of the laser beam and FBG element length setting (3 mm). The employed configuration is a gaussian standard profile (Figure 3.5).
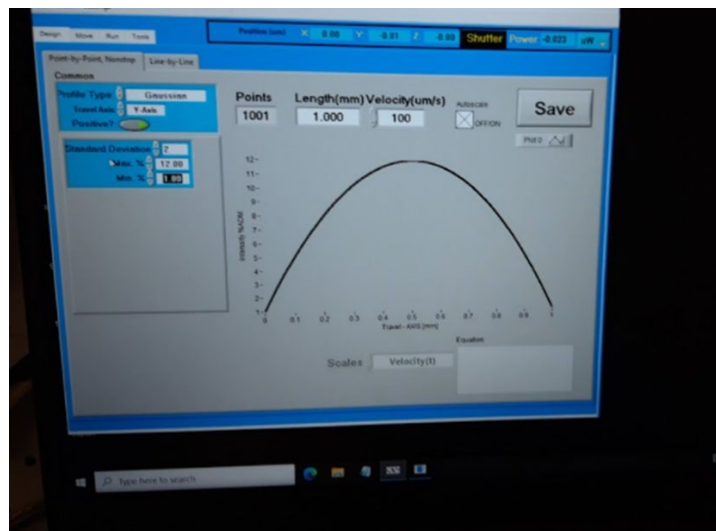

Figure 3.5: Laser's energy profile.

5) Setting of the stage speed, fixed to an empirical value of 99.78 μm/s.

The final optical fiber, with the 3-FBGs sensing elements embedded, is shown in Figure 3.6.
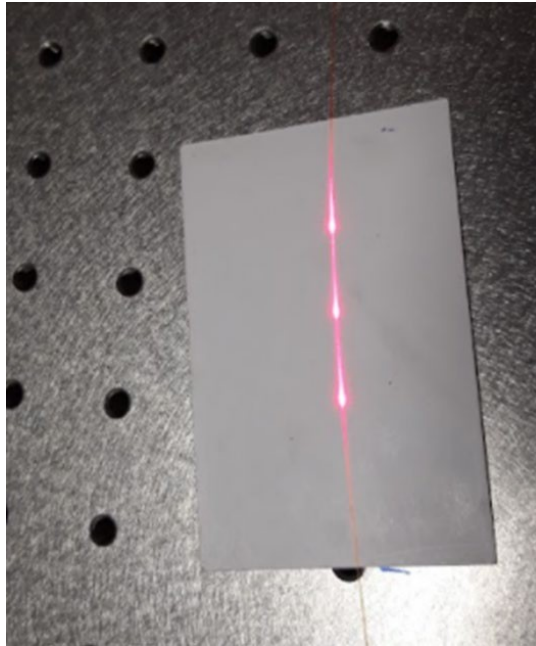
Figure 3.6: A single optical fiber with the 3-FBGs sensing elements embedded.

6) Wavelength final check: in the end of the process a final check is recommended to verify the gap between the desired wavelengths and the obtained ones. In this case the final reflection wavelengths are 1538.341 µm instead of 1538 µm for FBG1, 1548.904 µm instead of 1548 µm for FBG2 and 1557.880 µm instead of 1558 µm for FBG3. The three reflected spectrums (Figure 3.7), centred in the previous wavelengths, can be visualized using an optical spectrum analyser (OSA) like the MS9740A OSA by 'Anritsu' company.

Figure 3.7: The three reflected spectrums centred in the chosen wavelengths, related to the three FBGs elements.

1.1 Frame realization and final assembly

The Aluminium beam frame realization occurs at the Certema S.c.a.r.l. "Laboratorio Tecnologico Di Grosseto", using additive manufacturing technologies. In particular the Concept Laser M2 Cusing (in Figure 3.8), able to print different types of metals, is employed to realize the tool.

Figure 3.8 Concept Laser M2 Cusing.

This machinery is a "powder bed fusion" technology, which provides the controlled fusion of metallic powder grains under the action of heat. In this case, the heat source is a laser system, hence the technology is called "laser sintering". The machinery is composed of:

1) A laser system with laser diameter of 50 μm and laser power of 400 W
2) A powder tank with dimensions of 250 x 250 x 280 mm
3) A construction room with dimensions of 250 x 250 x 280 mm and a mechanism for powder spreading

The entire process occurs in a controlled environment. Critical parameters to check are temperature as well as the gas composition in the construction room. This is necessary because the employment of metallic powders involves the usage of an inert gas (Argon) to avoid the reaction between hot metal and oxygen.

The Concept Laser M2 Cusing has an accuracy of $\pm$ 100 μm, construction rate of 2-35 cm³/h with an obtainable layer thickness in the range 20-80 μm.

The material, initially in form of powder, is the CL 30AL Aluminium alloy (containing a 10% of Silicon) by General Electric (GE). The CL 30AL Aluminium alloy has a Young Module of $75*10^3$ N/mm^2 after the printing and a recommended heat treatment (this is the value considered in Section 3.2).

Because of constructive issues and to avoid a failure during the gluing fibers-frame procedure, the final Aluminium frame provided by Certema is quite different from the original design described in Section 2.10. In particular, the similar beam Aluminium frame has a thickness of 2.45 mm instead of 2 mm and the two through holes crossing along the metallic frame has a diameter of 800 μm instead of 300 μm. These changes are necessary to guarantee the assembly and gluing procedures, avoiding obstructions of the two holes.

The gluing procedure is implemented using a Cyanoacrylate-based glue because of adequate features in terms of viscosity. The fundamental request is that the glue must penetrate along the entire holes

to ensure an excellent fiber fixing. The final prototype (optical fibers integrated in the metallic frame) is presented in Figure 3.9.
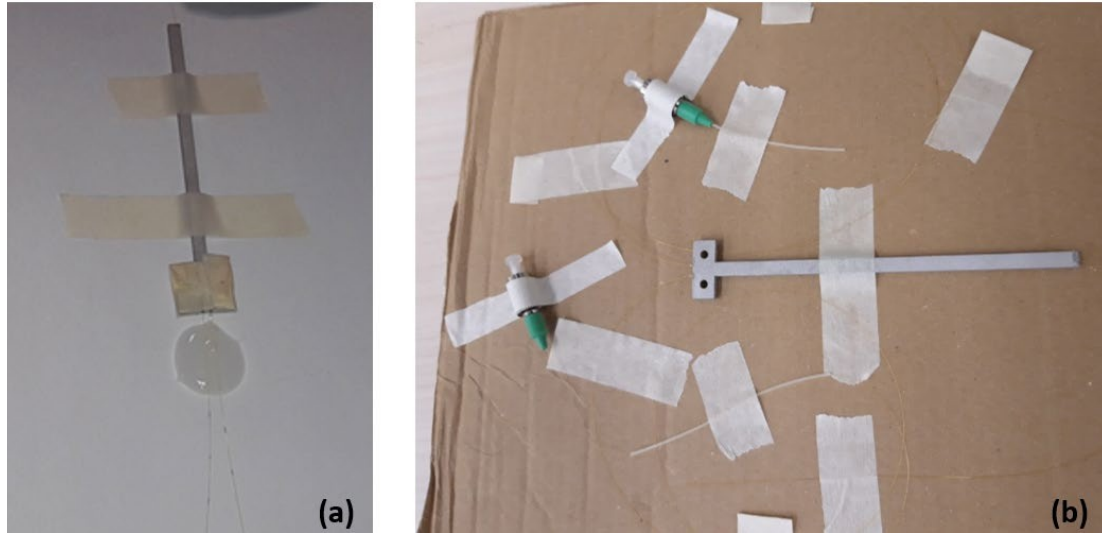

Figure 3.9: Gluing procedure (a) and final prototype (b) (optical fibers integrated in the metallic frame).

4. Tool experimental assessment

4.1 Design and fulfilment of the experimental Set-Up

In this Chapter, an experimental assessment of the previous prototype is proposed. The first step is the design of an experimental Set-Up, using Autodesk Fusion 360 Software, able to reproduce the simulated conditions and features of a gripping procedure. The second step is the fulfilment of ad-hoc components using additive manufacturing technologies in order to build the Set-Up. In the end, an experimental protocol is proposed as well as the final experimental results.

The experimental Set-Up should emulate the simulation conditions of the nodule gripping procedure exposed in Section 2.3, in order to validate the obtained results:

1) A force in the handle emulating the force exerted by user's fingertip, with an intensity in the range [0;10]N with a step of 1N, applied in a fingertip-similar square area of 6mm side length (handle_load input parameter).

2) Square's centre position along the tool major axis (y axis) in a range of [-10;0]mm with a step of 1 mm toward the tool middle line, in order to emulate the user's fingertip position (y_central input parameter).

3) Hemisphere/nodule centre position along the tool major axis (y axis) in a range of [57;47]mm with a step of -1 mm toward the tool's tip, in order to emulate different gripping positions (y_hemisphere input parameter). Moreover, reaction force on the nodule (Fz) -expressed in Newton (N)- should be detected for each parameters combination.

The experimental Set-Up design is implemented using Autodesk Fusion 360 Software (technical tables available in Appendix 1) and it is composed of:

(1) A precision vertical positioner 8MVT120-25 by 'standa' company (Figure 3.1), able to provide a high precision positioning along the z-axis.

Figure 3.1: Precision vertical positioner 8MVT120-25 by 'standa' company.

(2) An Aluminium base plate able to ensure the adequate work environment in light of the Set- Up components dimensions involved. Moreover, this element is necessary to guarantee ad- hoc links between the precision vertical positioner and the other Set-Up components.

(3) Two ad-hoc interfaces specifically 3D printed (Interface 1 and Interface 2), in order to customize the Aluminium base plate adapting it to the other Set-Up elements. Adequate housings for screws and screw-nuts are implemented too.

(4) A stable steel translation stage (called Stage 1) 7T67-25 by 'standa' company (Figure 3.2) with 25 mm travel range, able to provide a manual high precision positioning of the nodule along the y-axis of the prototype. This is essential to emulate different nodule gripping positions varying the y_hemisphere input parameter.

Figure 3.2: Stable steel translation stage (called Stage 1) 7T67-25 by 'standa' company.

(5) A load cell ATI Nano43. The ATI Nano43 Multi-Axis Force/Torque Sensor system measures all six components of force and torque. It is essential to measure the reaction force on the nodule (Fz).

(6) An ad-hoc interface specifically 3D printed (Interface 3), in order to connect the translational stage 'Stage 1' with the load cell. Screws housings have to be customized considering the lead cell specifications.

(7) A 3D printed probe with a soft silicon-based and hemispherical end, emulating the nodule.

(8) Two micro translation stages (called Stage 2 and Stage 3) model M-105 by 'Physik Instrumente (PI)' company (Figure 3.3) with 18 mm travel range mounted in a Y-Z configuration, able to provide a manual high precision positioning of the device along the y- axis as well as the z-axis. The displacement along the z-axis is essential to allow a device- nodule contact with different types of intensities. The z-axis mounting bracket for vertical mount of M-105 stages is necessary to allow the Y-Z configuration. Moreover, an adapting plate for the fixing of M-105 stage along the y-axis with the Aluminium base plate is necessary.

Figure 3.3: Translation stage (Stage 2 and Stage 3) model M-105 by 'Physik Instrumente (PI)' company.
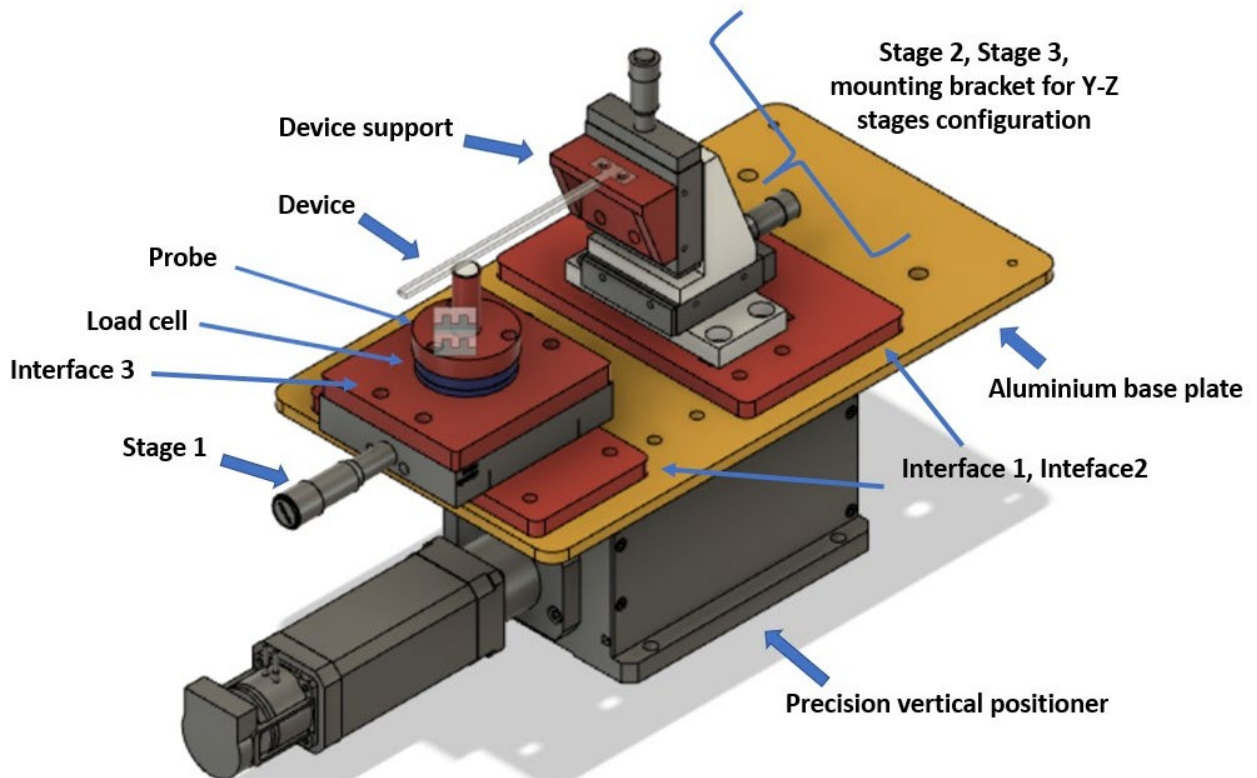
(9) A 3D printed device support, specifically customized based on the beam specifications, able to connect the prototype with PI translation stage (Stage 3) along the z-axis.

The entire CAD experimental Set-Up is displayed in Figure 3.4:

Figure 3.4: The entire CAD experimental Set-Up.

For a proper assembly of all the Set-Up components some screws and screw-nuts are necessary:

- 10 M3 screws
- 19 M6 screws
- 5 M3 screw-nuts
- 6 M6 screw-nuts

In the Set-Up assembly only simple or countersunk screws are employed while the screw-nuts use is necessary to fix Stage 1 with Interface 1, Interface 2 with the adapting plate for Stage 2 and the device with the device support.

Five Set-Up elements (Interface 1, Interface 2, Interface 3, Probe and the Device support) in red in Figure 3.4 have to be 3D printed while the other components (included the Aluminium base plate) are immediately available in the Laboratory. The employed 3D printer is an Ultimaker S5 printer (Figure 3.5), belonging to the fused deposition modelling (FDM) technology. The FDM process consists in the extrusion and subsequent deposition of a fused filament of polymeric material. The material filament is pushed towards a hot nozzle by some sprockets. After the extrusion, the material cools, leading to a hardening of the deposited filament with a return to the solid state. A weakness of this technology is the high printing time.
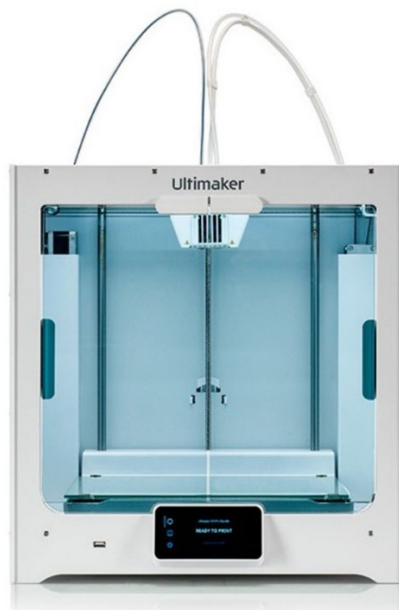
Figure 3.5: Ultimaker S5 printer.

The printing protocol is the same for each 3D element:

1) Creation of the CAD drawing with Autodesk Fusion 360 Software and saving in 'STL' format.
2) Uploading of the 'STL' file into the 'Cura' Software in order to set different printing parameters. The following parameters are valid for each element:
   - Material: PLA
   - Profile: 0.1 mm

- Shell: Wall Thickness 1.6 mm, Wall Line Count 4 layers, Top/Bottom Thickness 1mm, Top/Bottom layers 10
- Infill density: 40%
- Support: No support needed
- Build Plate Adhesion: Brim

3) Saving of the previous file in an 'UFP' format able to be read by the printer.

Moreover, a PLA model of the device is printed too, in order to verify the assembly correctness before mounting the original sensorized prototype.

The final experimental Set-Up, after the assembly, is proposed from different views in Figure 3.6:
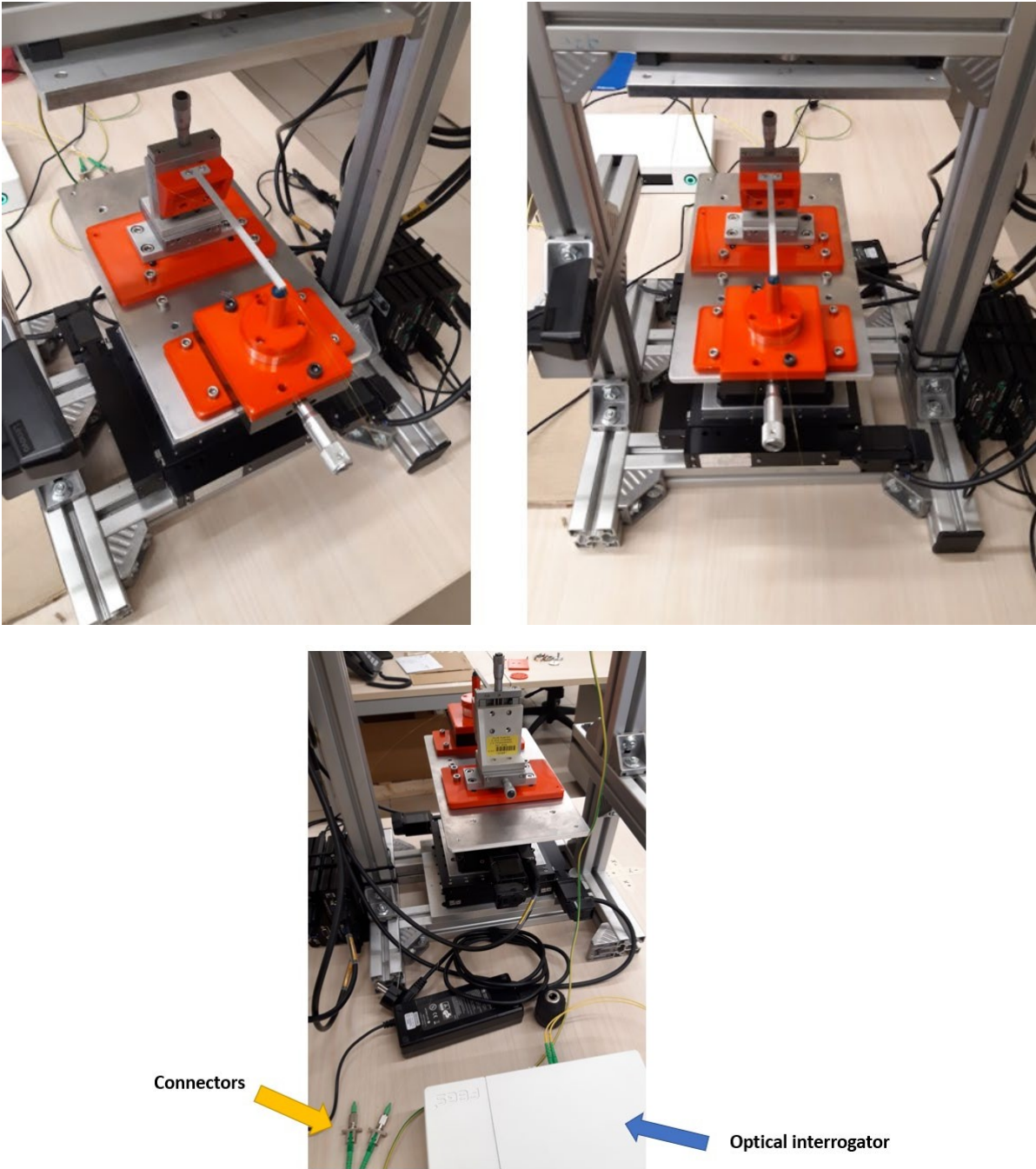
Figure 3.6: Different views of the final experimental Set-Up, after the assembly.

4.2 Experimental protocol

The proposed tool experimental evaluation follows a peculiar experimental protocol in order to collect adequate and robust results, able to implement the following experimental assessment.

A mandatory condition during the protocol drafting is the coherence with the FE analysis working conditions and features described in Chapter 2. The proposed experimental Set-Up is able to reproduce all the working conditions of the nodule gripping procedure considered in the FE analysis:

(1) A force in the handle emulating the force exerted by user's fingertip, with an intensity in the range [0:1:10] N, applied in a fingertip-similar square area of 6 mm side length.

(2) Square centre position along the tool major axis (y axis) in a range of [-10;0] mm with a step of 1 mm toward the tool's middle line, in order to emulate user's fingertip position.

(3) Hemisphere (nodule) centre position along the tool major axis (y axis) in a range of [57;47] mm with a step of -1 mm toward the tool tip, in order to emulate different gripping positions.

Despite of the designed Set-Up potentialities, the experimental assessment involves only the nodule centre position along the tool major axis (y-axis), initially positioning the probe on the tool tip and then moving it manually towards the tool handle using the stable steel translation stage 7T67-25 (Stage 1). The indentations cycles are powered moving manually the micro translation stage M-105 (Stage 2) along the z-axis in order to induce a tool-nodule contact.

The experimental protocol considers 33 total cycles of indentations, obtained by varying the position of the probe (and consequently of the silicon-based nodule) along the tool y axis, in six different points. For each probe position 3 cycles of indentations are repeated:

(1)   y_probe= 0 mm: 3 cycles of indentations
(2)   y_probe= 0.5 mm: 3 cycles of indentations
(3)   y_probe= 1 mm: 3 cycles of indentations
(4)   y_probe= 1.5 mm: 3 cycles of indentations
(5)   y_probe= 2 mm: 3 cycles of indentations
(6)   y_probe= 2.5 mm: 3 cycles of indentations
(7)   y_probe= 3 mm: 3 cycles of indentations
(8)   y_probe= 3.5 mm: 3 cycles of indentations
(9)   y_probe= 4 mm: 3 cycles of indentations
(10)   y_probe= 4.5 mm: 3 cycles of indentations
(11)   y_probe= 5 mm: 3 cycles of indentations

The data acquisition occurs at the Neuro-Robotic Touch Laboratory of The BioRobotics Institute (Scuola Superiore Sant'Anna). An optical interrogator FBG-Scan 90X (Figure 3.7) by 'FBGS' company is necessary to acquire experimental data, during the evaluation procedure, from the six FBGs sensors integrated in the tool. This machinery is able to work in a wavelength range 1510-1590 nm with four different optical channels, hence it is compliant with the project specifications. Moreover, two LC/APC adapters are necessary to link the optical interrogator with the two optical fibers terminations FC/APC. The optical interrogator is linked with a PC and the ILLumiSense Software v3.1.x – FBGS is employed to perform real time measurements.

Figure 3.7: Optical interrogator FBG-Scan 90X and optical fibers connectors.

4.3 Experimental assessment

Following the proposed experimental protocol, the data acquisition via optical interrogator is implemented using the measurement software ILLumiSense v3.1.x – FBGS (Figure 3.8). Two optical channels are employed because of the two different optical fibers with 3-FBGs elements inscribed. In Figure 3.8 are displayed the variations in terms of wavelength for each of the six FBGs elements (a single FBG is represented with a colour in order to identify the proper wavelength trend) during a nodule-tool indentation.

Each experimental session, in terms of cycles of indentations, is recorded. In the end of each different cycle, the measurement software provides two different 'txt' file, one for each channel (CH1/CH2), containing all the wavelength variations values related to the six FBGs sensors (3 FBGs for channel). Hence, in the end of the entire process a total number of 66 different files is provided to implement the final assessment.
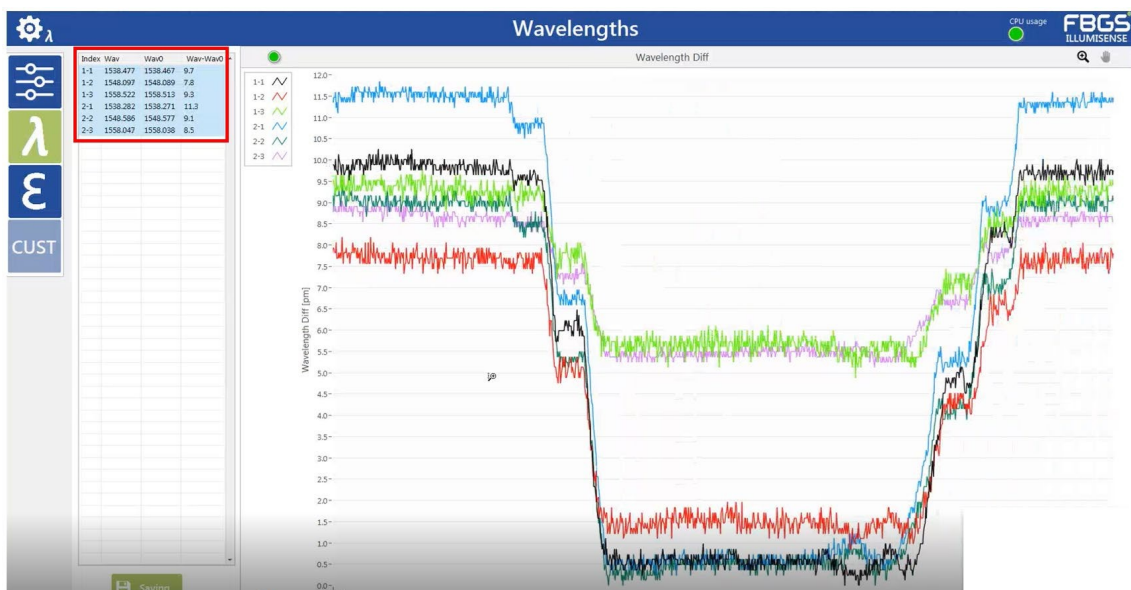
Figure 3.8: ILLumiSense Software, variations in terms of wavelength for each of the six FBGs elements.

The final step of the experimental evaluation involves the implementation of a Neural Network, using MATLAB Software, in order to obtain the performance of the six FBGs sensors in terms of reconstruction of the y_probe parameter (the probe position along the y-axis of the tool) and consequently the nodule position described in the previous Section, starting from the wavelength variations.

The NN dataset is composed by the 66 'txt' files achieved from the ILLumiSense Software, considering that a coupling of the two optical channels (CH1/CH2) is necessary to obtain a single file containing the wavelengths data referred to the 6 FBGs sensors.

Input and output of the Neural Network (NN):

- **NN Input**: A 515653x6 matrix, with a number of rows corresponding to each value of wavelength variation, detected with the optical interrogator, for each of the 33 files composing the NN dataset and a number of columns equal to the number of the FBGs sensors (Figure 3.9).

λ diff	FBG1	FBG2	FBG3	FBG4	FBG5	FBG6
1	Value	Value	Value	Value	Value	Value
2	Value	Value	Value	Value	Value	Value
3	Value	Value	Value	Value	Value	Value
4	Value	Value	Value	Value	Value	Value
.	.	.	.	.	.	.
.	.	.	.	.	.	.
.	.	.	.	.	.	.
515653	Value	Value	Value	Value	Value	Value

Figure 3.9: Input matrix (515653x6) of the Neural Network.

Each column of the Input matrix, containing the wavelength values related to a specific FBG in all the indentation cycles, can be plotted as a function of time dividing the number of samples by 1/(100 Hz) as in Figure 3.10.
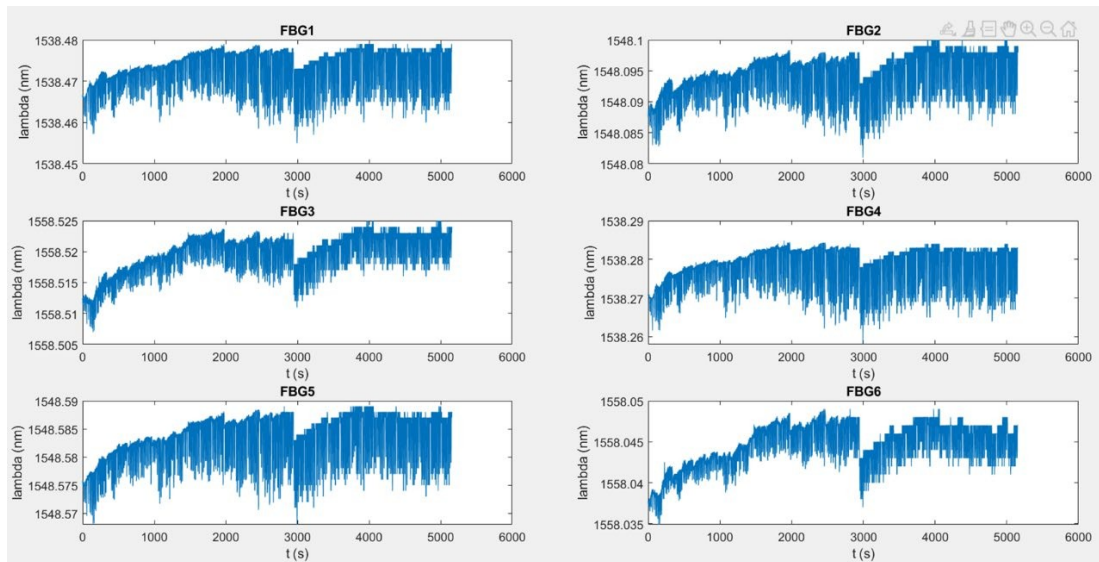
Figure 3.11: Plotted matrix columns.

- **NN Output:** A 515653x1 vector, with a number of rows corresponding to the total number of wavelength variations in the entire experimental process (33 cycles of indentations), containing the y_probe value related to the wavelength values (Figure 3.11).

	y_probe
1	Value
2	Value
3	Value
4	Value
.	.
.	.
.	.
515653	Value

Figure 3.11: Output vector (515653x1) of the Neural Network.

The entire starting dataset consisting of 33 '.txt' result files can be subdivided into three sub-categories:

(1) Training set: training ratio equal to 0.7
(2) Validation set: validation ratio equal to 0.15
(3) Testing set: validation ratio equal to 0.15

The dataset partition into the three sub-categories is totally random with the only ratios defined.
The proposed Neural Network has the same features of the NN described in Chapter 2.
The NN performance is evaluated in terms of Regression (R).
The NN regression plots as well as the error histogram are displayed in Figure 3.12. The R parameter is close to the value of 1, showing the training goodness and the capability of the proposed 6-FBGs sensors in detect the nodule position along the y-axis. Moreover, the NN error histogram shows a similar Gaussian trend with the maximum error (errors= targets-outputs) in the range [−0.2;0.2] mm. Hence, the proposed sensorized tool is able to detect a nodule with an error of 0.2 mm during a gripping procedure.
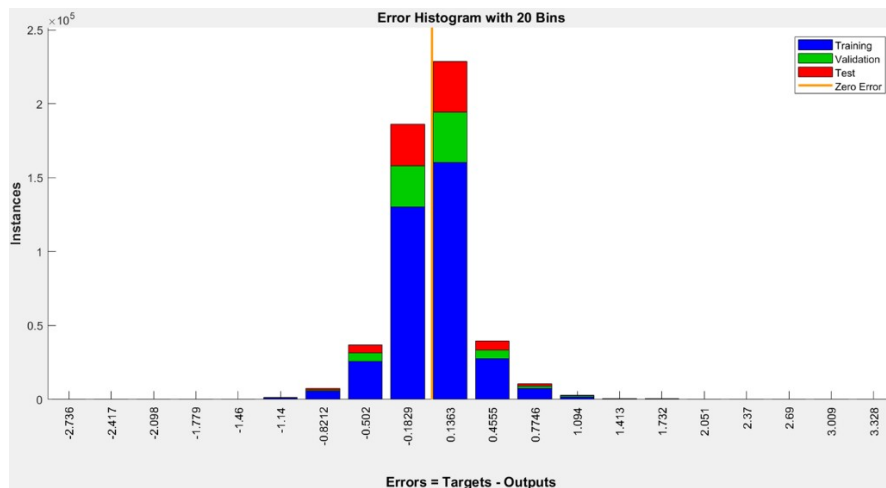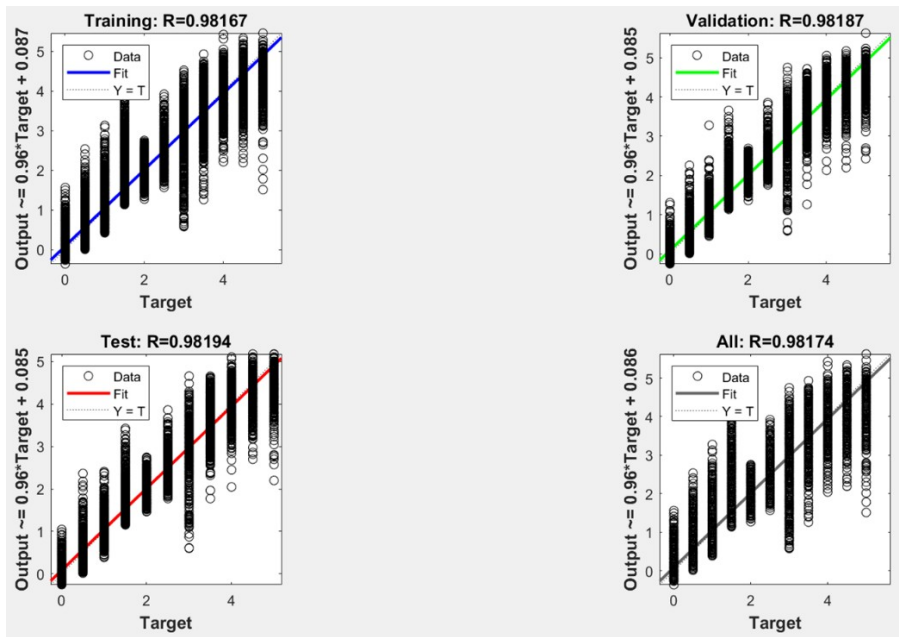
Figure 3.12: NN regression plots and NN error histogram.

The proposed surgical sensorized tool is able to detect the nodule-device contact during the grasping procedure with an accuracy of 200 μm, employing six FBGs sensors with the optimized positioning derived from the FEM analysis combined with the inverse modelling via Neural Networks.

The detection performance could be enhanced by inserting a threshold value of wavelength in order to highlight only when nodule and tool get in touch, instead of considering the entire dataset. As a consequence, the NN performance should improve as well as the capability in nodule position reconstruction.

5 Conclusions and future perspectives

The future vision will be the release of a new generation of smart surgical instruments with tactile and temperature sensing capacities interfaced to wearable haptic interfaces.

The design of instruments should be compatible for multiple tasks such as gripping, cutting, drilling, palpating, cauterizing. Variation in the design will enable hosting sensors.

The possibility to provide artificial sense of touch to the surgeon is expected to enormously impact surgical practice. The tactile information to be restored is a fundamental source of information for evaluation of clinical state of tissues and for controlling the surgical gesture.

From a medical perspective, the tactile information will prevent surgeons from accidentally applying excessive forces and damaging the treated tissue. Moreover, the sensorization of surgical tools will make MIS simulations more effective for trainees. Training with smart instruments will provide awareness of the forces being applied and the tissues being manipulated, leading to a shorter learning curve with a steadier upward

trend.

From a technological point of view, the integration of sensors in surgical tools will provide quantitative data for presenting haptic feedback to surgeons. This will allow improving the overall surgeon control and maneuverability of devices. The use of FOSs for multi-point force sensing will contribute overcoming challenges related to the application of electrical sensors in MIS, by developing final components either rigid (sensorized with FBGs) or flexible (sensorized with RBS) with waterproof, heat proof, and shock-proof properties and proper spatial resolution. FBG-based sensorization will improve the capabilities of conventional tools without considerable modification in terms of shape and dimensions. RBS, otherwise, will be used to develop a novel biomimetic flexible instrument for bringing up further enhancements to MIS tactile sensing applications by continuous tactile measurements. Finally, the integration of the temperature module with the surgical tools will bring knowledge about the influence of temperature in MIS

procedures (still underexplored) and foster the development of multifunctional tactile systems for MIS, to perform accurate and reliable force measurements by decoupling thermal and mechanical effects.

Such an instrumentation would address real-case scenarios, such as:

- Endoscopic surgery: this surgery is performed with endoscopic instruments that work without a pressure feedback for the surgeon: this surgery actually is based only upon endoscopic reduced images. The possibility to introduce sensors into these instruments will allow a better perception of surgery and an enhanced outcome.
- Neurosurgery: sensorized instruments will give advantage to brain surgery. In fact the possibility to measure mechanical and thermal forces will help to avoid iatrogenic lesions to healthy neural tissue, especially when treating tumors or vascular malformation making possible of avoid unwanted bleeding, unnecessary resections, shortening operation time, reducing risks of post-operative complications.
- Bone drilling surgery:t he possibility to insert haptic sensors inside bone drills could lead to a more accurate bone surgery.
- Zygomatic implants represent surgical interventions useful to restore fixed denture in edentulous patients with maxillar atrophy. This implant surgery unfortunately is related to many complications, as orbital impingement, zygomatic bone fracture and soft tissue

invasion. The possibility to introduce haptic sensors in bone drills could lead to a feedback bone drilling and safer surgery.

- Endovascular procedure: in endovascular procedures, catheters do not transmit mechanical properties of pathological or healthy tissues so that the surgeon cannot module pressure and strength so that the potential sensorization of catheters and probes can reduce iatrogenic risks and guarantee effective intervention.

- Training and simulation platform: the possibility with haptic sensors to measure pressure during surgical operations is a great matter of interest for students and residents in the training process. The simulation with sensorized instruments could be standardized in Universities and training courses, expectedly smoothing the surgical learning curve.

- Microsurgery and supramicrosurgery: micro and supramicrosurgical procedures require to handle micro instrumentation and suture, and address microscopic anatomical structures such as blood vessels or lymphatics. Having haptic sensors on a micro instrument will make each gesture more precise and safer. In addition, micro tactile feedback could be augmented via AI algorithms to amplify micro perception and make the gesture easier. The application could be extended also to robotic microsurgical procedures.

- Gynecology: medical assisted procreation is nowadays widely adopted. It requires in vivo embryo transfer with ecographic real-time monitoring. Releasing the embryo at the right position is essential. The currently adopted transfer probe cannot restitute tactile properties of the uterine tissue.

- Recording surgical gesture: the possibility of monitoring surgical gestures during operations in terms of mechanical and thermal forces applied by a surgeon represents a record of the procedure with a medical legal value in cases of trials about the adequacy of the surgical gesture.

Table of content: